A NUMERICAL MODELING STUDY OF THE MARINE BOUNDARY LAYER OVER THE GULF STREAM DURING COLD AIR ADVECTION

CHING-YUANG HUANG and SETHU RAMAN

Department of Marine, Earth and Atmospheric Sciences North Carolina State University Raleigh, NC 27695-8208, USA

(Received in final form 8 June, 1988)

Abstract. A two-dimensional mesoscale model has been developed to simulate the air flow over the Gulf Stream area where typically large gradients in surface temperature exist in the winter. Numerical simulations show that the magnitude and the maximum height of the mesoscale circulation that develops downwind of the Gulf Stream depends on both the initial geostrophic wind and the large-scale moisture. As expected, a highly convective Planetary Boundary Layer (PBL) develops over this area and it was found that the Gulf Stream plays an important role in generating the strong upward heat fluxes causing a farther seaward penetration as cold air advection takes place. Numerical results agree well with the observed surface fluxes of momentum and heat and the mesoscale variation of vertical velocities obtained using Doppler Radars for a typical cold air outbreak. Precipitation pattern predicted by the numerical model is also in agreement with the observations during the Genesis of Atlantic Lows Experiment (GALE).

1. Introduction

Sharp sea surface temperature gradients occur off the coast of the Carolinas during winters because of the existence of the Gulf Stream (Pietrafesa *et al.*, 1985) with a surface temperature of about 24 °C. A mid-shelf front normally occurs between the coastline and the western edge of the Gulf Stream due to the advection and diffusion processes caused by the Gulf Stream filaments. Very cold air with below-freezing near-surface temperatures advects over the warmer ocean causing significant convection (Atlas *et al.*, 1983). Cloud bands associated with these cold air outbreaks have been observed over the Gulf Stream (Chou and Atlas, 1982). One of the scientific objectives of the Genesis of Atlantic Lows Experiment (GALE) was to study the marine boundary-layer structure over the Gulf Stream during cold air outbreaks (Dirks *et al.*, 1987). Many boundary-layer observation systems such as meteorological buoys, research vessels, Doppler Radars and research aircraft were used during GALE to study the mean and turbulent structure of the marine boundary layer (Raman and Riordan, 1988). Semi-permanent rain bands were often observed (Hobbs, 1987) during the GALE field phase using lightning detectors and weather radars. Existence of these rainbands is believed to be due to the formation of a sea breeze-type of circulation and associated convergence near the western edge of the Gulf Stream.

Boundary-Layer Meteorology **45** (1988) 251–290.

The purpose of this paper is to examine the air mass modification over the coastal waters and the Gulf Stream during a typical cold air advection using a two-dimensional mesoscale numerical model with a first-order closure scheme and compare different predicted variables such as mean velocities, surface turbulent fluxes and precipitation patterns with observations during GALE under similar synoptic conditions.

2. Model Description

2.1. Model equations

After Reynolds decomposition and ensemble averaging for the governing equations of basic flow with Boussinesq's assumptions and the transformation of vertical coordinate to terrain following coordinate σ, the governing equations are given by (Huang, 1986)

$$\frac{\partial u}{\partial t} = -u\frac{\partial u}{\partial x} - v\frac{\partial u}{\partial y} - \tilde{w}\frac{\partial u}{\partial \sigma} + fv - \theta\frac{\partial \pi}{\partial x} - g(1-\sigma)\frac{\partial E}{\partial x} - g\sigma\frac{\partial H}{\partial x} + \frac{\partial}{\partial x}\left(K_H\frac{\partial u}{\partial x}\right) + \frac{\partial}{\partial y}\left(K_H\frac{\partial u}{\partial y}\right) + \frac{1}{H-E}\frac{\partial}{\partial \sigma}(\overline{-u'w'}), \tag{1}$$

$$\frac{\partial v}{\partial t} = -u\frac{\partial v}{\partial x} - v\frac{\partial v}{\partial y} - \tilde{w}\frac{\partial v}{\partial \sigma} - fu - \theta\frac{\partial \pi}{\partial y} - g(1-\sigma)\frac{\partial E}{\partial y} - g\sigma\frac{\partial H}{\partial y} + \frac{\partial}{\partial x}\left(K_H\frac{\partial v}{\partial x}\right) + \frac{\partial}{\partial y}\left(K_H\frac{\partial v}{\partial y}\right) + \frac{1}{H-E}\frac{\partial}{\partial \sigma}(\overline{-v'w'}), \tag{2}$$

$$\frac{\partial \theta}{\partial t} = -u\frac{\partial \theta}{\partial x} - v\frac{\partial \theta}{\partial y} - \tilde{w}\frac{\partial \theta}{\partial \sigma} - \delta\frac{L}{\pi}\frac{\mathrm{d}q_s}{\mathrm{d}t} + \frac{\partial}{\partial x}\left(K_H\frac{\partial \theta}{\partial x}\right) + \frac{\partial}{\partial y}\left(K_H\frac{\partial \theta}{\partial y}\right) + \frac{1}{H-E}\frac{\partial}{\partial \sigma}(\overline{-w'\theta'}), \tag{3}$$

$$\frac{\partial q}{\partial t} = -u\frac{\partial q}{\partial x} - v\frac{\partial q}{\partial y} - \tilde{w}\frac{\partial q}{\partial \sigma} + \delta\frac{\mathrm{d}q_s}{\mathrm{d}t} + \frac{1}{H-E}\frac{\partial}{\partial \sigma}(\overline{-w'q'}), \tag{4}$$

$$\frac{\partial \pi}{\partial \sigma} = -\frac{g(H-E)}{\theta}, \tag{5}$$

$$\frac{\partial u}{\partial x} + \frac{\partial v}{\partial y} + \frac{\partial \tilde{w}}{\partial \sigma} = \frac{1}{H-E}\left(u\frac{\partial E}{\partial x} + v\frac{\partial E}{\partial y}\right) - \frac{1}{H-E}\left(\frac{\partial H}{\partial t} + u\frac{\partial H}{\partial x} + v\frac{\partial H}{\partial y}\right), \tag{6}$$

where primes denote fluctuating quantities.

Equations (1) and (2) are the momentum equations for east-west velocity (u) and north-south velocity (v) components respectively, Equation (3) is the thermodynamic equation for potential temperature (θ), Equation (4) is the conservation equation for moisture (q), Equation (5) is the hydrostatic equation for

scaled pressure (π) and Equation (6) is the mass continuity equation for the computation of vertical velocity ($\tilde{w}$) in the σ coordinate system defined as

$$\sigma = \frac{z - E(x, y)}{H(x, y, t) - E(x, y)},$$

where $E(x, y)$ is terrain height and $H(x, y, t)$ is the total height of the model domain. The scaled pressure from Exner's function is defined as

$$\pi = C_p(p/p_{00})^{R/C_p},$$

where the reference pressure p_{00} is 1000 mb.

Note that Equations (1), (2) and (3) have the explicit diffusion terms with K_H as the horizontal eddy diffusivity. These terms are used to suppress the nonlinear instability caused by aliasing error (Pielke, 1974a).

We can relate w to $\tilde{w}$ as

$$w = \tilde{w}(H-E) - (\sigma - 1)\left(u\frac{\partial E}{\partial x} + v\frac{\partial E}{\partial y}\right) + \sigma\left(\frac{\partial H}{\partial t} + u\frac{\partial H}{\partial x} + v\frac{\partial H}{\partial y}\right). \tag{7}$$

The total height H could be made prognostic and derived from the continuity equation as

$$\frac{\partial H}{\partial t} = -\int_0^1 \left(\frac{\partial u(H-E)}{\partial x} + \frac{\partial v(H-E)}{\partial y}\right) d\sigma - \tilde{w}_T(H-E), \tag{8}$$

where $\tilde{w}_T$ is $\tilde{w}$ at the model top. For the present study, the height of the model domain was fixed since the sea breeze-type of circulation is essentially shallow.

Total change of saturated water vapor given by the term $\delta\, dq_s/dt$ in the moisture equation is derived from the Clausius–Clapeyron equation and is approximately given by

$$\frac{dq_s}{dt} = \frac{-gC_pq_s(LR - \theta\pi R_v)w}{R(R_v\theta^2\pi^2 + C_pq_sL^2)}, \tag{9}$$

and the symbol δ is such that

$$\delta = \begin{cases} 1, & \text{if } w > 0 \text{ and } q \geq q_s \\ 0, & \text{otherwise.} \end{cases}$$

Precipitation in the model is calculated by the relation,

$$P = \int_t^{t+\Delta t}\int_0^1 -C_pp_{00}(\pi/C_p)^{C_p/R}\frac{(H-E)}{R\pi\theta}\delta\frac{dq_s}{dt}\,d\sigma\,dt. \tag{10}$$

Definition of the symbols used in this paper is given in the Appendix.

Since the sea/land breeze system is a thermally driven direct circulation, it is probably better to integrate the hydrostatic equation from the surface to the model top. The required tendency equation of the surface-scaled pressure (π_s)

from the continuity equation is then given by

$$\frac{\partial \pi_s}{\partial t} = -\int_0^1 g(H-E)\frac{1}{\theta^2}\frac{\partial \theta}{\partial t}\,\mathrm{d}\sigma\,. \tag{11}$$

Note that the surface pressure change is related to the total net heating in a column. The surface temperature changes are specified based on the observational data.

2.2. Closure schemes

To close the governing equations, unknown turbulent flux terms are required to be specified by mean fields. The similarity relationships given by Businger *et al.* (1971) are used for the surface layer in the model. For the outer layer of the PBL, it has been found that the K-dynamics method has the problem of expressing the variation of the eddy diffusivity K in regions of counter-gradient fluxes in a convective boundary layer (Deardorff, 1966). Second-order closure schemes are probably better to describe the turbulent properties; however, several studies have found (e.g., Yamada and Mellor, 1975; McNider and Pielke, 1981) no substantial difference in the results between the two closure schemes in a mesoscale model. In the present study, a first-order closure scheme is used to simulate the cold air advection over the Gulf Stream. Parameterization schemes used in the model for different layers of the PBL are discussed below.

(a) *Surface Layer*

The similarity relationships which work at the medium stability ranges were examined for the wind field. In the breeze type of circulation, mean flow becomes very weak near the location of the upward limb where the strongest heat fluxes occur. This is also the region where calm winds prevail in the presence of strong unstable conditions. Many similarity relationships would fail under conditions of near-zero wind. A proper specification for minimum u_* is reasonable in a numerical simulation (Pielke and Mahrer, 1978) and this value is assumed to be $0.01\ \mathrm{cm\,s^{-1}}$. The roughness length z_0 over the sea is given by Charnock's relationship (Clark, 1970) of the form

$$z_0 = 0.018\frac{u_*^2}{g}\,. \tag{12}$$

Although the coefficient in the above equation has been found to be somewhat variable, a value of 0.018 is used in the model (Arya, 1988). Roughness length z_0 is prescribed as 4 cm over land. Also, a minimum value of 0.000015 m is imposed on the z_0 based on observations (Raman and Raynor, 1975). Though the roughness length over land is highly variable, the simulation results are not very sensitive to the slight roughness changes (Pielke, 1974a, b) since the circulation develops over the sea several kilometers downwind of the coastline.

The expressions for u_*, θ_* and q_* are then given by

$$u_* = kV/[\ln(z/z_0) - \Psi_M(z/L)], \tag{13}$$

$$\theta_* = k(\theta - \theta_{z0})/[0.74(\ln(z/z_0) - \Psi_H(z/L))], \tag{14}$$

$$q_* = k(q - q_{z0})/[0.74(\ln(z/z_0) - \Psi_H(z/L))], \tag{15}$$

where u_*, θ_* and q_* are friction velocity, flux temperature and flux moisture, respectively. In the above relationships, the integral functions $\Psi_M(z/L)$ and $\Psi_H(z/L)$ are given by

$$\Psi_M(z/L) = \begin{cases} 2\ln[(1+\phi_M^{-1})/2] + \ln[(1+\phi_M^{-2})/2] - 2\tan^{-1}(\phi_M^{-1}) + \pi/2 & z/L \le 0 \\ -4.7z/L & z/L > 0, \end{cases}$$

and

$$\Psi_H(z/L) = \begin{cases} 2\ln[(1+0.74\phi_H^{-1})/2] & z/L \le 0 \\ -6.35z/L & z/L > 0, \end{cases}$$

and relationships for ϕ_M and ϕ_H are given by

$$\phi_M = \frac{kz}{u_*}\frac{\partial V}{\partial z} = \begin{cases} (1-15z/L)^{-1/4} & z/L \le 0 \\ 1+4.7z/L & z/L > 0, \end{cases}$$

and

$$\phi_H = \frac{kz}{\theta_*}\frac{\partial \theta}{\partial z} = \begin{cases} 0.74(1-9z/L)^{-1/2} & z/L \le 0 \\ 0.74+4.7z/L & z/L > 0, \end{cases}$$

where

$$V^2 = u^2 + v^2.$$

In the above functions, z/L is a non-dimensional stability parameter and the Monin–Obukhov stability length L is defined as

$$L = \frac{\bar{\theta} u_*^2}{kg\theta_*},$$

where $\bar{\theta}$ is the average air temperature near the surface.

The values of θ and q at height z_0 are assumed (Zilitnkevich, 1970; Deardorff, 1974) as

$$\theta_{z0} = \theta_s + 0.0962(\theta_*/k)(u_* z_0/\upsilon)^{0.45}, \tag{16}$$

and

$$q_{z0} = q_s + 0.0962(q_*/k)(u_* z_0/\upsilon)^{0.45}, \tag{17}$$

where subscript s denotes the value at the surface. Fluxes of momentum, heat

and moisture are parameterized as

$$\overline{u'w'} = -K_M \frac{\partial u}{\partial z} = -u_*^2 \cos u \,, \tag{18}$$

and

$$\overline{v'w'} = -K_M \frac{\partial v}{\partial z} = -u_*^2 \sin \mu \,, \tag{19}$$

where $\arctan(v/u) = \mu$

and

$$\overline{w'\theta'} = -K_\theta \frac{\partial \theta}{\partial z} = -u_* \theta_* \,, \tag{20}$$

$$\overline{w'q'} = -K_q \frac{\partial q}{\partial z} = -u_* q_* \,. \tag{21}$$

Once u_*, θ_* and q_* are determined, the surface fluxes are known.

(b) *Transition Layer*

The vertical profile of K values in the transition layer is computed by a cubic interpolation scheme given by O'Brien (1970),

$$K(z) = K_{z_i} + [(z_i - z)/(z_i - z_{h_s})]\{K_{h_s} - K_{z_i} + (z - h_s)\left[\frac{\partial K_{h_s}}{\partial z} + 2\frac{(K_{h_s} - K_{z_i})}{(z_i - h_s)}\right]\} \quad z_i \geq z \geq h_s \,, \tag{22}$$

where z_i is the height of the PBL and h_s is the height of the surface layer assumed to be related to z_i as

$$h_s = 0.04 z_i \,. \tag{23}$$

The coefficient 0.04 in Equation (23) is based on observations in a neutrally-stratified boundary layer (Blackadar and Tennekes, 1968). The interpolation scheme given by Equation (22) has been used in mesoscale models for its reasonable representation of the variation of eddy diffusion coefficient with height (Pielke and Mahrer, 1975). One of the shortcomings of this method is that it depends only on two levels given by z_i and h_s and tends to give a maximum value of K near one third of z_i. A linear K profile (Estoque, 1961) was also employed to compare the results with those using the cubic scheme. Numerical results indicate that the cubic interpolation work better, resulting in a more intensified circulation at upper levels of the PBL, but the basic patterns of PBL structures for the two schemes are very close. A value of $0.1\ \mathrm{m^2\ s^{-1}}$ is specified for K_{z_i}.

(c) *The Height of PBL*

Variation of the height of the PBL is modeled using the relationship suggested by Deardorff (1974) for convective conditions as

$$\frac{\partial z_i}{\partial t} = -u_{z_i}\frac{\partial z_i}{\partial x} - v_{z_i}\frac{\partial z_i}{\partial y} + w_{z_i} + \frac{[1.8(w_*^3 + 1.1u_*^3 - 3.3u_*^2 f z_i]}{\left(g\frac{z_i^2}{\theta_{h_s}}\frac{\partial\theta^+}{\partial z} + 9w_*^2 + 7.2u_*^2\right)}, \tag{24}$$

where $\partial\theta^+/\partial z$ is the potential temperature gradient above the PBL and w_* is defined as

$$w_* = \begin{cases} \left(-\frac{g}{\theta_{h_s}} u_* \theta_* z_i\right)^{1/3} & \theta_* \leq 0 \\ 0 & \theta_* > 0. \end{cases}$$

In the above equations, θ_{h_s} is the potential temperature at the top of the surface layer. This prognostic equation for z_i that includes the effects of entrainment is generally used in predicting the height of a well mixed boundary layer. However, a highly convective PBL characterized by large w_* does not normally have a steady state for z_i as found in the present study and such conditions normally have strong updrafts. Equation (24) generally tends to overpredict the height of PBL under these conditions. The height of PBL could also be estimated by examining the vertical temperature profile similar to the method used by Anthes (1978). Another alternative is to use higher order closure schemes (e.g., Yamada and Mellor, 1975). Nevertheless, some recent simulations of mesoscale circulation using Equations (24) and (22) (e.g., Pielke and Mahrer, 1975) have shown reasonable results.

2.3. Finite difference schemes

The model equations are integrated using a forward-upstream scheme on a non-staggered finite-difference mesh in which all variables are defined at the same grid. The derivatives of the pressure and flux terms are computed by central differencing schemes of second order except for the boundaries where a first-order scheme is used. The finite-difference forms of the governing equations are not presented here for brevity.

The upstream scheme for the advection term has already been examined by several authors (e.g., Pielke, 1974a, b; Mahrer and Pielke, 1978) who found that this scheme is sufficient to simulate a convective-dominant circulation with little loss of important features. We arrive at the same conclusion (not shown here) by comparing the results using a more elaborate scheme such as the quadratic upstream scheme (Leonard, 1979) and the modified upstream scheme suggested by Smolarkiewicz (1983).

The vertical diffusion terms for subgrid-scale fluxes are represented by an implicit scheme (Mahrer and Pielke, 1978),

$$\frac{\phi_k^{n+1}-\phi_k^n}{\Delta t}=\frac{1}{\Delta z_k}\left[K_{k+1/2}\frac{\alpha(\phi_{k+1}^n-\phi_k^n)+\beta(\phi_{k+1}^{n+1}-\phi_k^{n+1})}{\Delta z_{k+1/2}}\right.$$
$$\left.-K_{k-1/2}\frac{\alpha(\phi_k^n-\phi_{k-1}^n)+\beta(\phi_k^{n+1}-\phi_{k-1}^{n+1})}{\Delta z_{k-1/2}}\right].$$

We found that the implicit scheme given above allows a much larger time step to obtain almost the same results as that using an explicit scheme if $\alpha = 0.25$ and $\beta = 0.75$ for one-dimensional vertical diffusion for a given potential temperature profile over Grid 25 at the western boundary of the Gulf Stream. Also, the implicit scheme assists in reducing the numerical instability that could be caused by a vertically-stretched grid mesh. Brown and Pandolfo (1979) showed using a linear analysis that a strong downdraft from a coarse mesh into a fine mesh could increase the numerical instability even for an implicit scheme. However, we did not encounter instability when the time step was increased to a value twenty times larger than that permitted for an explicit scheme. This is believed to be due to the weak downdraft in a breeze-type circulation and the moderate stretching of grid mesh in our model. The implicit scheme needs an interpolated lower boundary value consistent with the transport of surface fluxes by similarity relationships. The lower boundary values can be obtained using Equations (18) to (21).

2.4. Initial conditions

To obtain the initial fields for the numerical simulations, the following equations for momentum, temperature and pressure are considered for the steady state solution:

$$\frac{\partial u}{\partial t}=fv-\theta\frac{\partial \pi}{\partial x}+\frac{1}{(H-E)}\frac{\partial}{\partial \sigma}(\overline{-u'w'}), \tag{25}$$

$$\frac{\partial v}{\partial t}=-fu-\theta\frac{\partial \pi}{\partial y}+\frac{1}{(H-E)}\frac{\partial}{\partial \sigma}(\overline{-v'w'}), \tag{26}$$

$$\theta\frac{\partial \pi}{\partial x}=fV_g(\sigma), \tag{27}$$

$$\theta\frac{\partial \pi}{\partial y}=-fU_g(\sigma), \tag{28}$$

$$\theta=\theta_s+\gamma(H-E), \tag{29}$$

$$\frac{\partial \pi}{\partial \sigma}=-\frac{g(H-E)}{\theta}, \tag{30}$$

where γ is the lapse rate and θ_s is the surface potential temperature. In the set of equations above, $U_g(\sigma)$, $V_g(\sigma)$ are the zonal and longitudinal geostrophic wind components, respectively. Lapse rate γ is specified as 3.85 °C/km and values of U_g and V_g vary according to cases studied. The initial model height is 5500 m and the value of Coriolis parameter f used in the model is for 35° latitude. A uniform surface potential temperature is specified first and the vertical profile is then obtained using Equation (29). Initially, the surface layer is assumed neutral and the surface roughness uniform (4 cm in all simulations). Height of the PBL is determined by the steady state solution of Equation (24) using a first guess from the relation $z_i = 1.1u_*/(3.3f)$ for neutral condition. Using Equations (27), (28) and (30), the geostrophic wind is known and Equations (25) and (26) are solved. A solution is considered to have been obtained when the total relative error of all vertical layers is below 0.1% for both u and v.

2.5. Boundary conditions

(a) *Lateral Boundary Conditions*

For the outflow grids of the lateral boundaries, the variables are computed by the Equations (1) to (4) using forward-upstream differencing. This is equivalent to a partial smoothing for the grids close to the boundaries. Some numerical models (e.g., Sun and Hsu, 1988) with a leapfrog scheme tended to apply an upstream scheme to the grids nearest to the boundary to accomplish smoothing instead of an explicit smoother or filter. For the inflow grids, we use the radiation boundary condition suggested by Orlansky (1976). When applying the forward-upstream scheme for the interior grids, Orlansky's scheme uses the same format as suggested by Miller and Thorpe (1981), who pointed out that it is more accurate to use an upstream-forward scheme as compared to a leapfrog scheme. However, it has been found (Physick, 1976) that the simulations of breeze type of circulation are not sensitive to the lateral boundary conditions. We conducted many numerical experiments with zero-gradient boundary conditions and found that the results (not shown here) are almost identical to those using the radiation conditions. Similar results were also obtained by others (Physick, 1976; Mahrer and Pielke, 1978). Nevertheless, we decided to implement this radiation condition for its simplicity and the reduction in computer time. For pressure, the horizontal gradients in the lateral boundaries are unchanged, which leads to the existence of geostrophic balance rather than the hydrostatic balance. Since we allow the developed circulation to move out of the domain, the vertical velocities are not specified for the inflow and the outflow grids.

(b) *Lower Boundary Conditions*

At the lower boundary, a no-slip condition is imposed for the wind. For the surface temperature, a typical horizontal variation observed during GALE has been used (see Figure 1). For the land surface, relative humidity remains

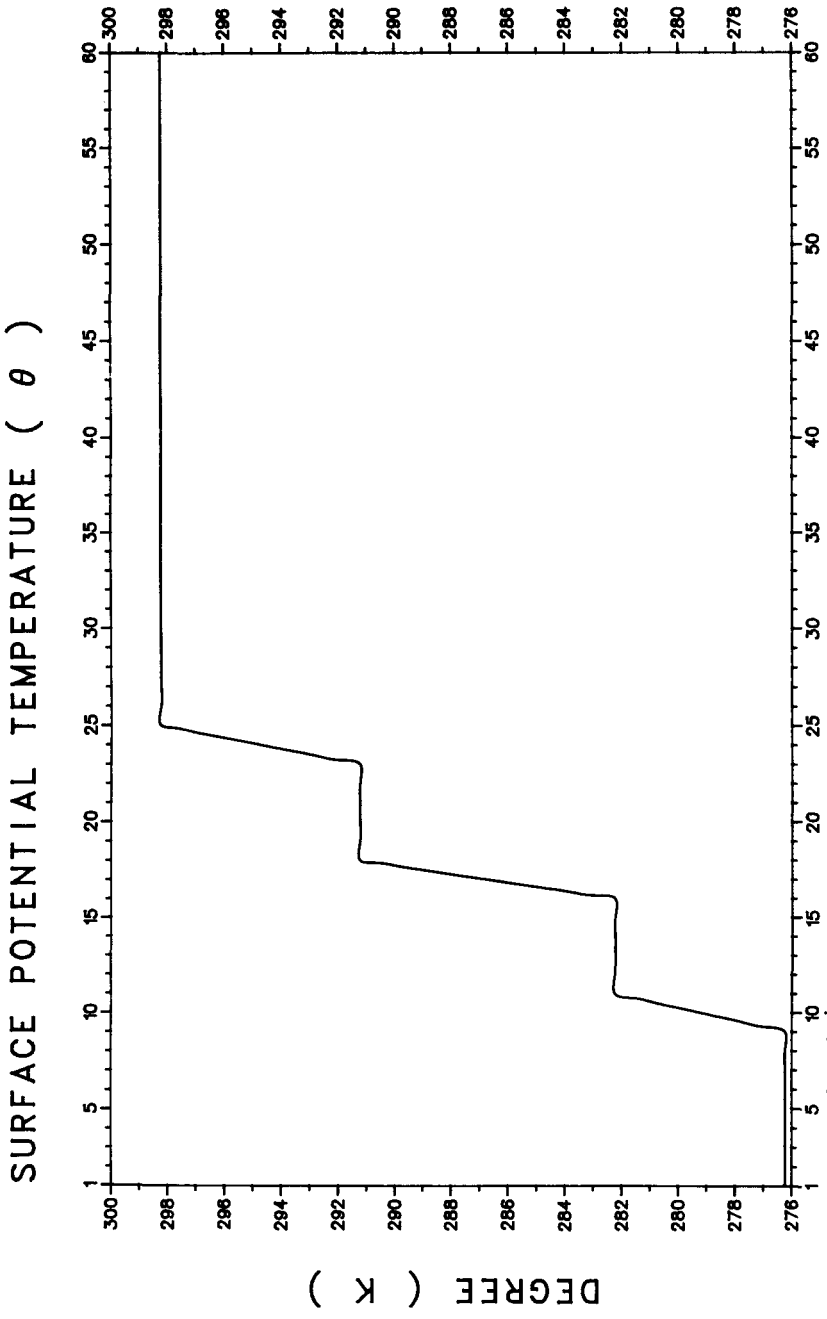

Fig. 1. Spatial distribution of surface potential temperature after four hours of adjustment time. MSF and G.S. represent Mid-Shelf Front and the Gulf Stream respectively and the grid interval is 10 km.

unchanged, but the air in contact with the sea surface is assumed to be saturated. Surface pressure is computed by the tendency Equation (11).

(c) *Upper Boundary Conditions*

For the upper boundary conditions, prognostic variables such as u, v, θ and q are computed by prediction Equations (1), (2), (3) and (4) respectively, using the forward-upstream differencing scheme for the outflow grids. For the inflow grids ($w < 0$), u, v, θ and q have the same treatment except for the vertical gradient which is represented by the interior grid nearest the boundary using upstream differencing. The pressure field at the upper boundary is unchanged when the hydrostatic equation is integrated downward. We shall show in a later section that downward integration and upward integration for the hydrostatic equation give similar results.

2.6. Grid System and Model Parameters

The horizontal grid interval is 10 km for all cases. Total height of the model domain is 5.5 km where a pressure of 500 mb is imposed initially. There are 16 vertical layers at 0, 50, 100, 150, 200, 250, 300, 400, 600, 900, 1300, 1800, 2500, 3500, 4500, and 5500 m. Choice of these vertical spacings is not critical in numerical simulations because of the use of an implicit scheme for the vertical diffusion terms. The intersection of land and sea is located at grid number 10, the mid-shelf oceanic front at grid number 18 and the Gulf Stream at grid number 25. The horizontal gradient of sea surface temperature is approximately 22 °C/150 km (see Figure 1) which is large compared with values reported in the breeze type of studies. This gradient corresponds to a typical surface temperature distribution observed off the Carolinas during a cold air outbreak (Raman and Riordan, 1988).

The integration time interval is 60 s for all cases. With due consideration for numerical instability and the spurious gravity waves that might be excited by pulse heating, sea surface temperatures are increased gradually to the distribution shown in Figure 1 in 2 hr and the integration is terminated at 7 hr after the sea surface temperature distribution is fixed. Before introducing the surface heating, a one-hour adjustment time is allowed for the changes in surface roughness for land and water. There is no diurnal variation of sea surface temperature in the model domain. An integration time of 7 hr was chosen from consideration of a typical land-sea breeze heating cycle as an average value. We recognize that the imposed integration period is rather arbitrary, however the net heating problem associated with a heavy density current will not permit a steady state solution (Smith and Lin, 1982; Lin and Smith, 1986). We also checked this situation by running several cases with an integration time of more than 20 hr and found that the behaviour of the density current tends to advect downstream and eventually moves out of the computational domain. Radiative cooling and the diurnal and

noctural variation of temperature will also become important for a longer time integration.

To evaluate and integrate the model equations with time, the momentum equations are computed first, the thermodynamic equation using the updated horizontal wind is computed second which is then followed by the moisture equation and the continuity equation and finally the hydrostatic equation and then the smoothing, if needed.

2.7. Numerical smoothing

Most of the mesoscale numerical models used some smoothing to obtain a reasonable result without sacrificing the intensity and structure of the dynamic system. Physically, energy cascade from the mean fields to the subgrid scales takes place through eddy dissipitation in the inertial subrange. This process is not readily solvable even in a microscale model. Thus the use of smoothing can be regarded as a parameterization of the turbulent transfer of energy to smaller scales. An explicit smoother or filter is also important for the removal of some correct but unwanted features of the solution such as internal gravity waves; the smoother also reduces the computational errors, in particular the aliasing, and maintains numerical stability. A suitable choice of smoothing tool is thus important (Shapiro, 1971, 1975; Cullen, 1976). The smoother or the filter applied in our model is discussed below.

(a) *Nonlinear Explicit Smoother*

The horizontal eddy transfer coefficient in Equations (1), (2) and (3) is an important parameter used to maintain computational stability. A nonlinear dynamic process suggested by Leith (1969) for K_H is more powerful than the conventional linear diffusion. One of the variable nonlinear dynamic forms for the coefficient K_H as used by Pielke (1974a, b) can be chosen as

$$K_H = \alpha \Delta x \Delta y \left\{ \left(\frac{\partial v}{\partial x} + \frac{\partial u}{\partial y} \right)^2 + \frac{1}{2} \left[\left(\frac{\partial u}{\partial x} \right)^2 + \left(\frac{\partial v}{\partial y} \right)^2 \right] \right\}^{1/2}, \tag{31}$$

where α is a coefficient chosen for a specific simulation and usually has a value of order one.

(b) *Linear Filter*

The linear filter (Shapiro, 1971) used in the model is given by

$$\overline{\phi_i} = (1 - S)\phi_i + \frac{S}{2}(\phi_{i+1} + \phi_{i-1}),$$

where ϕ_i is a variable at grid number i and S is a numerical filtering coefficient. This filter is applied twice: first with $|S|$ and second with minus $|S|$ as two individual procedures. This filter has little damping on the wavelengths larger than 8 ΔX and completely removes the 2 ΔX waves if $S = 0.5$ (Shapiro, 1971,

1975; Physick, 1976). It could be made equivalent to a linear explicit diffusion scheme with an appropriate choice of K_H (Shapiro, 1971). A very selective low-pass filter using an implicit form rather than this simple one is also used by other mesoscale models (e.g., Mahrer and Pielke, 1978b; Sun and Hsu, 1988) because of the additional advantage of very little damping effect on 4 ΔX waves for a given Courant number. However, as discussed by Pielke (1984), various Courant numbers existing in computational processes make complete control of selective damping impossible. Since the effects of the linear filter are most concentrated in the region of smaller scales, a higher resolution for a numerical model becomes important if the scale of the most pronounced magnitudes in a simulation is essentially small. Under this condition, experiments of the energy cascade by turbulent transfer are beyond the scope of this paper. However, it is important to understand the overall variations in the PBL for typical cold air advection over a warm region.

As discussed above, the selection of a particular numerical method is very important for the accuracy of the simulations, so we performed several numerical control experiments. Nine basic runs of the numerical control experiments were selected to study the effects of smoothing in a nonlinear system and in addition to compare upward and downward integrations of the hydrostatic equation. We applied the linear filter at each time step using two procedures with a linear increase of S (given $S = 0$ at the bottom and $S = 0.5$ at the top) to the three layers nearest to the upper boundary. The three layers could be considered as a slightly absorbing zone for the divergence of the wind caused by the integration of the hydrostatic equation.

2.8. Numerical control experiments

It is important to determine the error growth in any numerical simulation in relation to the numerical techniques used in a model. The ultimate test would be to compare the model results with the observations. Fortunately, for this study extensive mesoscale observations made during GALE are available for comparison. The solution of a sea-breeze type circulation depends much on the nonlinear processes involving surface turbulent fluxes which in turn will depend on the complicated step function for the sea surface temperature near the Gulf Stream. In order to separate the numerical factors from the effects of the sharp temperature gradient near the western edge of the Gulf Stream, the step increase of the sea surface temperature near the Gulf Stream was removed and the moist convection ignored.

Several experiments were conducted with the above surface boundary conditions using different digital filters and modes of integration of the hydrostatic equation. Choice of parameters, filter types and methods of integration used for these control experiments are given in Table I. Four experimental runs with very low winds, two with moderate winds and three with strong winds were made. Very low geostrophic wind with $U_g = V_g = 0.1\ \mathrm{m\,s^{-1}}$ was chosen to study the

TABLE I

The numerical tests for the smoothing and the integration of the hydrostatic equation. The surface differential heating is specified as in Figure 1 but with the removal of the one temperature step over the Gulf Stream area.

Tests	Geostrophic wind	Smoother or filter	Integration of the hydrostatic equation
Run 1	$U_g = 0.1$ m/s $V_g = 0.1$ m/s	Nonlinear smoother with $\alpha = 500$	Upward for a given surface pressure computed by Equation (11)
Run 2	$U_g = 0.1$ m/s $V_g = 0.1$ m/s	Linear filter applied once per every one time step	Same as Run 1
Run 3	$U_g = 0.1$ m/s $V_g = 0.1$ m/s	Linear filter applied twice per every two time steps	Same as Run 1
Run 4	$U_g = 0.1$ m/s $V_g = 0.1$ m/s	Linear filter applied twice per every two time steps	Downward
Run 5	$U_g = 2.5$ m/s $V_g = 0.1$ m/s	Linear filter applied once per every two time steps	Same as Run 1
Run 6	$U_g = 2.5$ m/s $V_g = 0.1$ m/s	Linear filter applied once per every ten time steps	Downward
Run 7	$U_g = 10$ m/s $V_g = 0.1$ m/s	Nonlinear smoother with $\alpha = 5$	Same as Run 1
Run 8	$U_g = 10$ m/s $V_g = 0.1$ m/s	Linear filter applied once per every fifteen time steps	Same as Run 1
Run 9	$U_g = 10$ m/s $V_g = 0.1$ m/s	Linear filter applied once per every twenty time steps	Downward

convection-dominated nonlinear effects. Other conditions were chosen to be consistent with the eventual numerical simulation of the cold air advection to be discussed in Section 3. Important results such as maximum vertical velocities, wind speeds and seaward penetration of the circulation cell for different runs are given in Table II.

Numerically generated waves exist aloft for run 1 in the wind field even when a large value of 500 is used for the horizontal diffusion coefficient α; however the pattern of potential temperature aloft is quite smooth. We also ran the same case of run 1 with $\alpha = 100$ and found that the disturbed waves occur in the potential temperature fields as well. The pronounced differences, however, disappear for runs 2 and 3, which implies that the ability of the linear filter is superior to the

TABLE II

The maximum vertical velocities (w), horizontal wind speeds (u) and seaward penetrations of all Runs. The surface differential heating is specified as Figure 1 but with the removal of the one temperature step over the Gulf Stream area.

Tests	Vertical velocity (w) (cm/s)	Wind speed (u) (m/s)	Seaward penetration (km)
Run 1	5.4	0.42	Not well defined
Run 2	0.6	0.69	110
Run 3	0.6	0.70	110
Run 4	0.6	0.71	110
Run 5	2.3	4.23	160
Run 6	4.9	4.54	150
Run 7	2.9	11.8	Not well defined
Run 8	2.8	11.9	Not well defined
Run 9	2.6	12.0	Not well defined

nonlinear smoother. The latter obviously becomes less efficient when the wind is very weak. Results from run 4 indicate that the downward integration of the hydrostatic equation gives better results than the use of Equation (11) with the upward integration in spite of using an absorbing zone for the latter. As suggested by Physick (1976), the disturbances generated near the upper boundary by the pressure gradients can be removed using a strong damping filter to the upper layers at every time step with a value of 0.5 for S, but it could suppress the physical processes related to the release of latent heat aloft. A comparison of the results of all runs indicates that smoothing applied at every ten times steps gives essentially similar results for higher wind speeds where nonlinearity is not as much as for lower wind speeds. This comparison strongly suggests that a reliable smoothing routine should be used that will suppress the computational or aliasing errors but not damp the dynamic system. The nonlinear smoother becomes more effective for the case with higher wind speed (run 7) and in this case the linear filter need not be used too frequently to obtain a reasonable simulation (run 8). The results for run 9 show that the simulation is not sensitive to upward or downward integration of the hydrostatic equation for a stronger geostrophic wind.

Results from the above nine control numerical experiments provided important information related to the numerical techniques for the solution of breeze-type circulation. However, the inherent implicit diffusion produced by an upstream scheme which is proportional to the wind speed and grid size complicates the selection of the best smoother or filter. Weaker damping schemes such as the quadratic upstream scheme and the modified upstream scheme discussed in Section 2.3 are designed to serve a wide range of simulations, but the upstream scheme is efficient to simulate a convective PBL (Mahrer and Pielke, 1978). For the numerical simulations of cold air advection over the Gulf Stream discussed in

Section 3, we decided to use the linear filter because of its superiority in handling numerical errors. An explicit smoother may be more appropriate for the numerical simulation of tropical cyclones because of its better representation of wind gradients (Cullen, 1976). In addition, a slightly absorbing zone using the filter with $S = 0.25$ and $S = -0.25$ is also used in order to minimize the reflective waves from the lateral boundaries. As discussed before, a breeze-type circulation exists over the Gulf Stream area far from the lateral boundaries of the model domain.

2.9. Simulated cases

Four cases are chosen for different background flows and humidities:

Case 1. Geostrophic wind U_g is $2.5\ \mathrm{m\,s^{-1}}$ and the relative himidity (RH) in each layer is 80%.

Case 2. U_g is $10\ \mathrm{m\,s^{-1}}$ and the RH is 80% in each layer.

Case 3. U_g is $2.5\ \mathrm{m\,s^{-1}}$ and the RH is 80% at the surface, then linearly decreases to 10% at the top of model.

Case 4. Same as Case 3 except that U_g is $10\ \mathrm{m\,s^{-1}}$.

The geostrophic component, V_g is set to be $0.1\ \mathrm{m\,s^{-1}}$ in all cases. We could have considered a larger V_g to investigate the effects of Coriolis force on the breeze-type circulation; however, the purpose of this paper is to simulate the thermally induced circulation over the Gulf Stream area. Vertical profiles of the initial potential temperature are the same in all cases as discussed in Section 2.4. It is also assumed that the initial surface layer is neutral and that the air at the sea surface is saturated for all cases. The linear filter is applied twice for every ten times steps (10 min), which is similar to the one used by Physick (1976).

3. Discussion of Results

3.1. Convergence zones

Figures 2a, 2b, 2c and 2d are the simulation results of the wind fields for Cases 1, 2, 3 and 4, respectively. Vertical component of the wind vector has been exaggerated by a factor of two with respect to the east-west component. Referring to Case 1 in Figure 2a ($U_g = 2.5\ \mathrm{m\,s^{-1}}$ and RH = 80%), there is an acceleration of the horizontal wind beginning from the land-sea interface (Grid #10) with the most pronounced effect near the Gulf Stream edge (Grid #25). The convergence caused by the sea-breeze type of circulation is most prominent about 50 km downwind of the western edge of the Gulf Stream. The surface temperature discontinuities at the land-sea interface (Grid #10) and the mid-shelf front cause increases in horizontal wind speed, but no convergence with significant vertical velocities is observed. Major convergence occurring at 50 km downwind of the Gulf Stream is associated with a maximum vertical velocity of

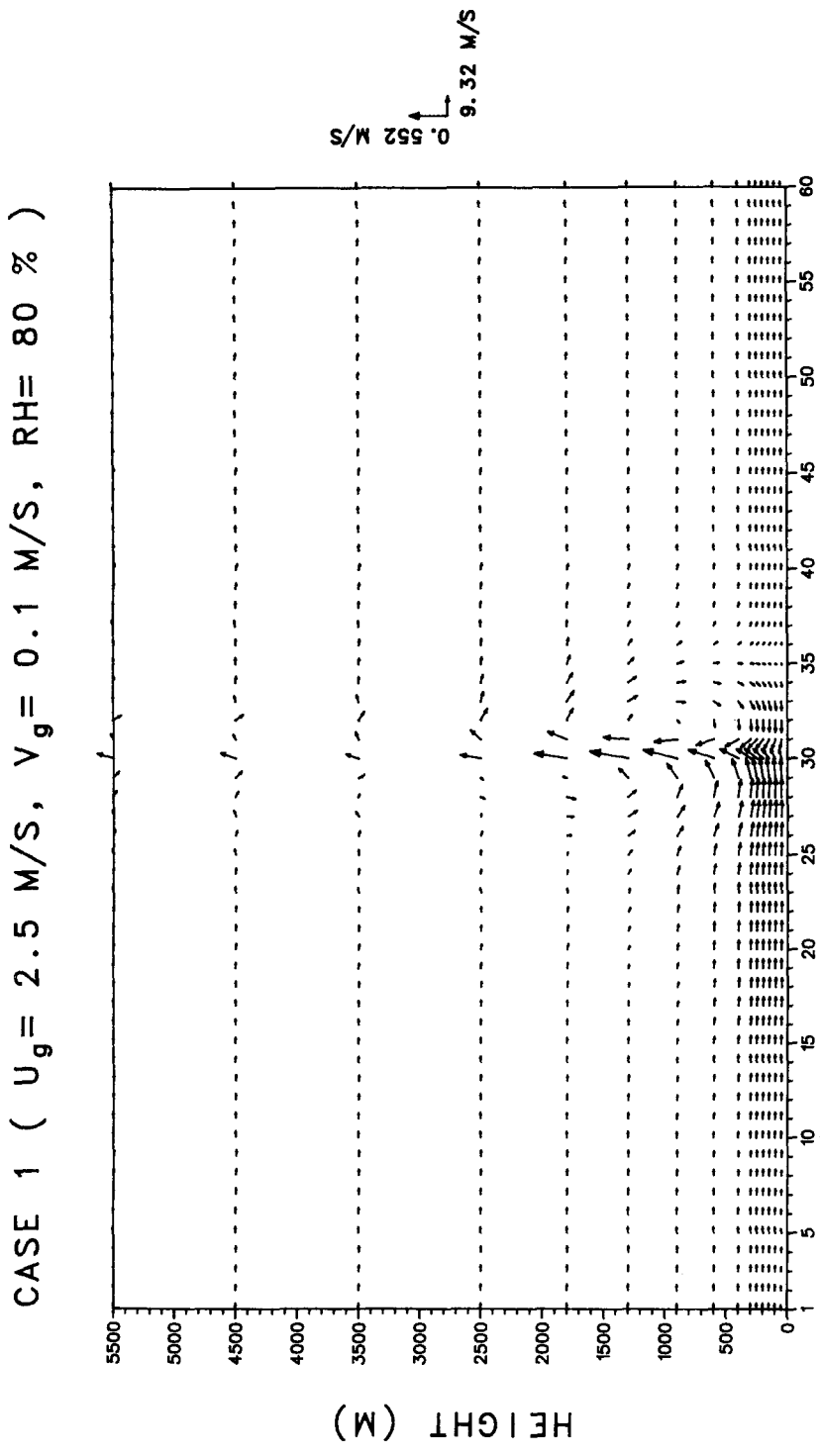

Fig. 2a. Wind vector for Case 1 (see Section 2.9) for u and w at 7 hr simulation time after the sea surface temperature was fixed. Maximum values of u and w are plotted at the right-hand edge.

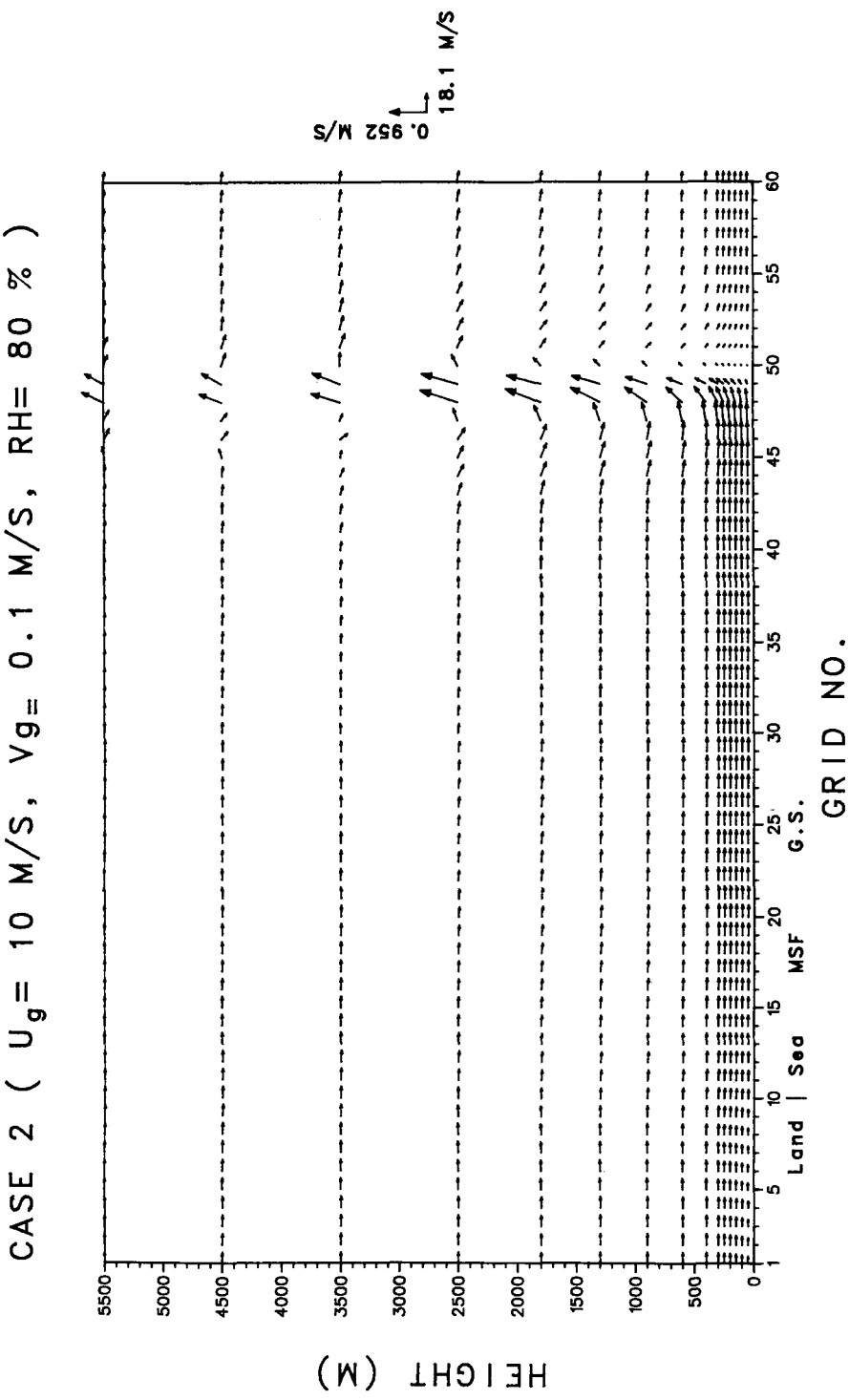

Fig. 2b. Same as Figure 2a but for Case 2 (see Section 2.9).

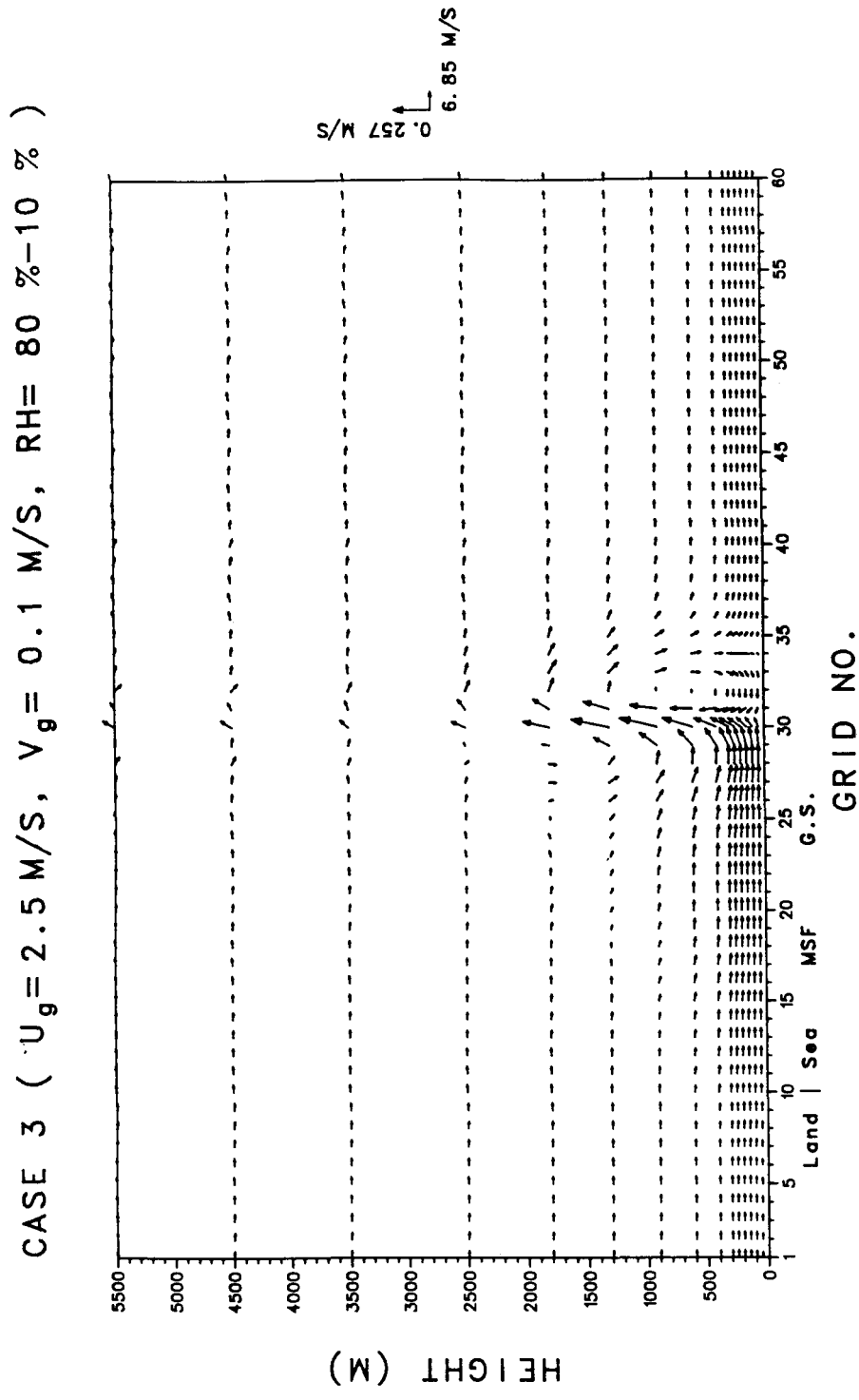

Fig. 2c. Same as Figure 2a but for Case 3 (see Section 2.9).

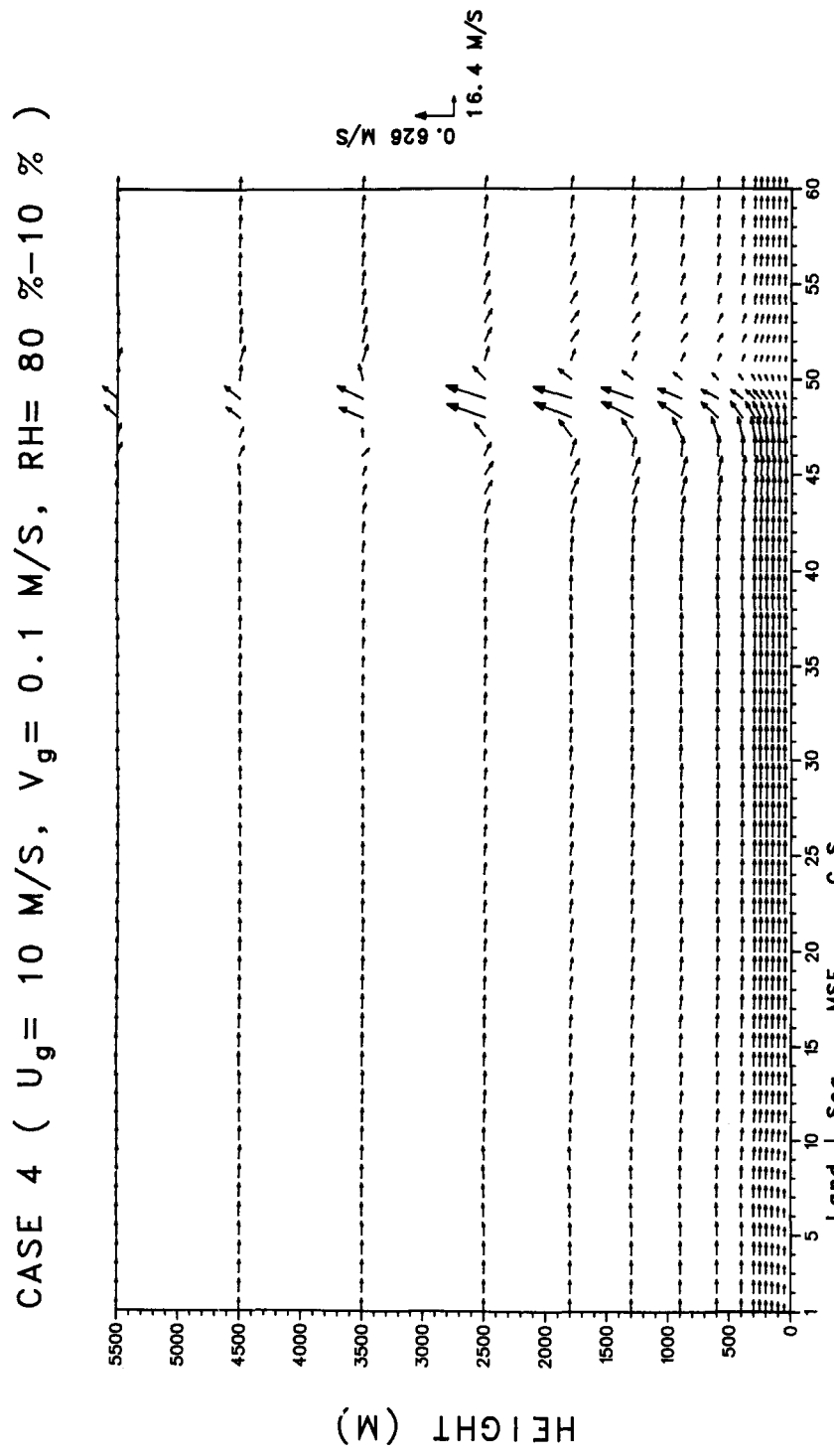

Fig. 2d. Same as Figure 2a but for Case 4 (see Section 2.9).

55 cm s^{-1} occurring at a height of about 1 km and a maximum horizontal wind speed of 9.3 m s^{-1} just before the convergence. This corresponds to an increase of the horizontal wind speed by about a factor of almost four. Effect of convergence as seen by vertical velocities extends to the entire height of the domain. There is no obvious return flow associated with the convergence zone since the ambient flow is in the direction of the increasing surface temperature.

Figure 2b shows the model results for Case 2 ($U_g = 10$ m s^{-1} and RH = 80%) where the geostrophic wind has been increased by a factor of four but the distribution of moisture is the same as in Case 1. Convergence in this case occurs at about 230 km (Grid #48) downwind of the western edge of the Gulf Stream as compared to about 50 km downwind in Case 1 (Figure 2a). The distance has increased by about a factor of four, consistent with the increase in geostrophic wind. As before, the major convergence occurs downwind of the Gulf Stream with no apparent effect at the other two temperature discontinuities. This feature might be because of the cumulative baroclinic effect of the sea-surface temperature discontinuities. Horizontal wind speeds increase with a maximum value of about 18 m s^{-1}, again an increase by a factor of 1.8 as compared to about 4 in the first case. Vertical velocities are larger with a maximum value of 95 cm s^{-1} and the effect of convergence on the wind field is seen up to the height of the domain (~5.5 km) with maximum values of vertical motion at about 2.5 km. Wind speeds associated with a typical cold air outbreak are usually of the order 10 m s^{-1} (Raman *et al.*, 1985).

Model results for Case 3 ($U_g = 2.5$ m s^{-1} and RH varying from 80 to 10% in the vertical) are shown in Figure 2c. The convergence occurs at about the same downwind distance as in Case 1, but the associated vertical velocities are much weaker with a maximum value of only 26 cm sec^{-1}. Increase in horizontal velocities near the surface caused by the temperature difference is essentially similar but with a lower maximum value of 6.9 m s^{-1} as compared to 9.3 for Case 1. With an increase in large-scale wind speed to 10 m sec^{-1} but with the same initial moisture distribution, results are similar as shown in Figure 2d. Maximum horizontal wind speed is slightly smaller (16.4 m s^{-1}) as compared to 18.1 m s^{-1} in Case 2, and the vertical velocities associated with the convergence are again slightly reduced to 63 cm s^{-1}. Thus the vertical distribution of background moisture appears to be important in the release of latent heat at upper levels and in increasing the magnitude of convergence near the western edge of the Gulf Stream.

Vertical velocities across the Gulf Stream for a moderate cold air outbreak on March 2, 1986, during GALE were about 50 cm s^{-1}. The distribution of the vertical velocities were obtained from dual Doppler Radar measurements using Chaff dispersal in the PBL (Marshall and Raman, 1986). Maximum values of model vertical velocities shown in Figure 2b are in general agreement with the observations. Also the distribution of the area of positive and negative vertical velocities is similar to the observations.

3.2. Air mass modification

Variation of the height of the internal boundary layer with distance offshore is shown in Figure 3. At large downwind distances, the internal boundary layer normally merges with the PBL. More enhanced growth resulting in a maximum height of the boundary layer occurs for Case 2 with stronger wind (U_g = 10 m s^{-1}) and higher moisture (RH = 80%) initial conditions. The increase is smooth except near Grid #48 where a sharp peak is observed corresponding to the region of increased vertical velocities (see Figure 2b). Variation of boundary-layer height for Case 4 with U_g = 10 m s^{-1} and linearly decreasing RH is similar to Case 2. Such a sharp change is probably associated with strong cumulus convection near the western edge of the Gulf Stream during cold air advection and has been observed during GALE by the airborne mission scientists. A PBL height of about 2700 m was observed at an offshore distance of about 160 km over the Gulf Stream during the cold air outbreak of January 28, 1986 (Wayland and Raman, 1987). This is in agreement with the model values shown in Figure 3 where a PBL height of 2700 m is reached at an offshore distance of about 200 km.

Case 1 (U_g = 2.5 m s^{-1} and a uniform RH of 80%) and Case 3 (U_g = 2.5 m s^{-1} and linearly decreasing RH) show similar variation of z_i as discussed above except that the heights are less by about a factor of two with the z_i reaching an equilibrium value closer to the western edge of the Gulf Stream. The peaks in z_i for these two cases are associated with the convergence zones and significant vertical velocities (see Figure 2a for Case 1). For the linearly decreasing RH (Case 3), the peak at Grid #30 corresponds with the convergence pattern shown in Figure 2d. Decrease in the equilibrium boundary-layer height to 1500 m is believed to be due to decreased surface heat fluxes.

Contours of the potential temperatures for the four cases are shown in Figures 4a to 4d. All cases show a highly convective PBL developing over the ocean. Height of the convective PBL is well defined in the vertical profiles of the potential temperatures inferred from these figures. For Cases 1 and 3 with a lower wind speed, the maximum height of the convective PBL is about 1.9 km, while for Cases 2 and 4 with a higher wind speed, the maximum height is about 3.6 km, which is about a factor of two higher. For all cases, location of the maximum height of the convective PBL developing over the warmer water corresponds to the location of the maximum vertical velocity. Addition of the upper moist condition in Cases 1 and 2 clearly produces a more pronounced limb of potential temperature aloft as compared with Cases 3 and 4. This obviously indicates the effect of increased latent heat release. Thus, initial moist conditions play an important role in supplying additional heat to the upper level flow; however, low-level structure of the PBL does not change much. About 10 °C modification of air temperature has been caused by the strong upward heat flux over the the location of the maximum height of PBL for all cases, but a sharp

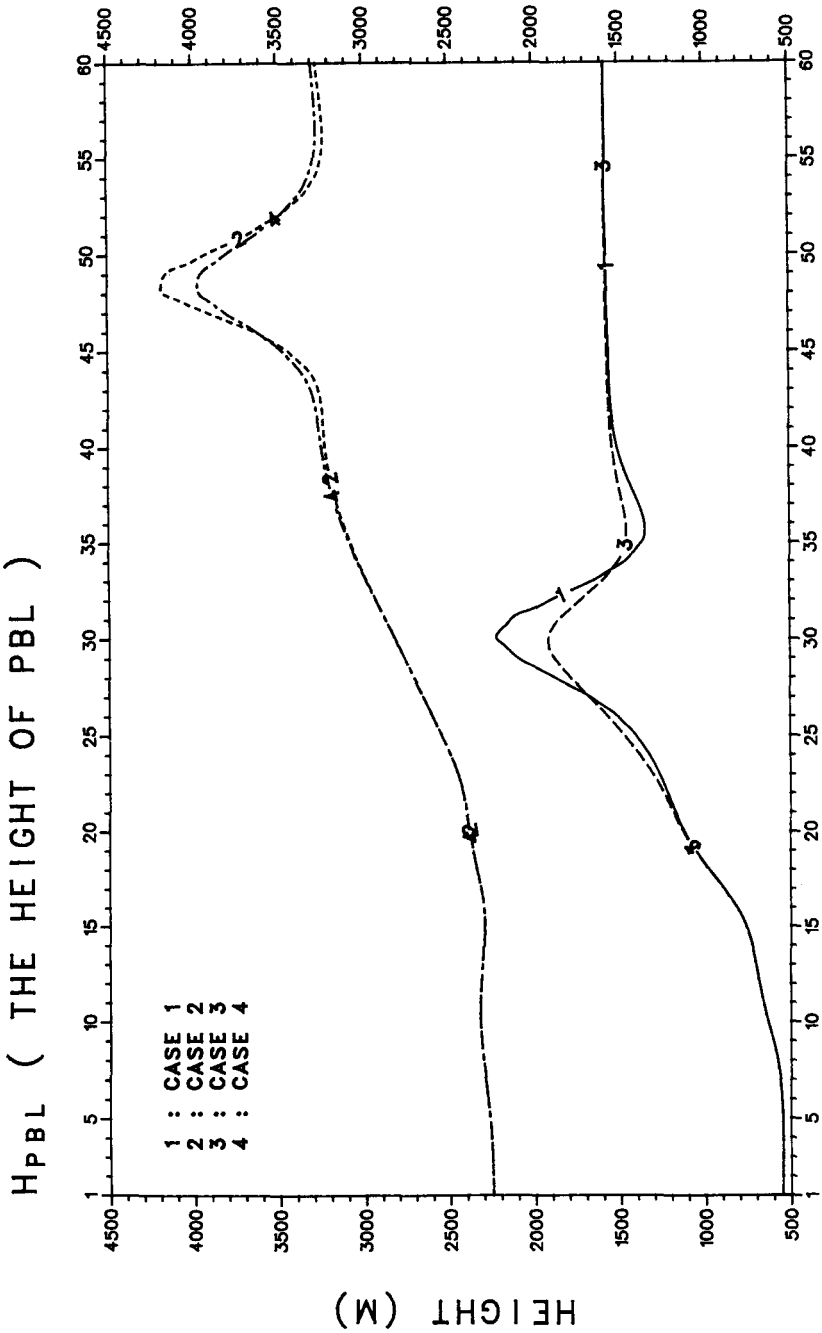

Fig. 3. Height of PBL for the four cases at 7 hr after the sea surface temperature was fixed.

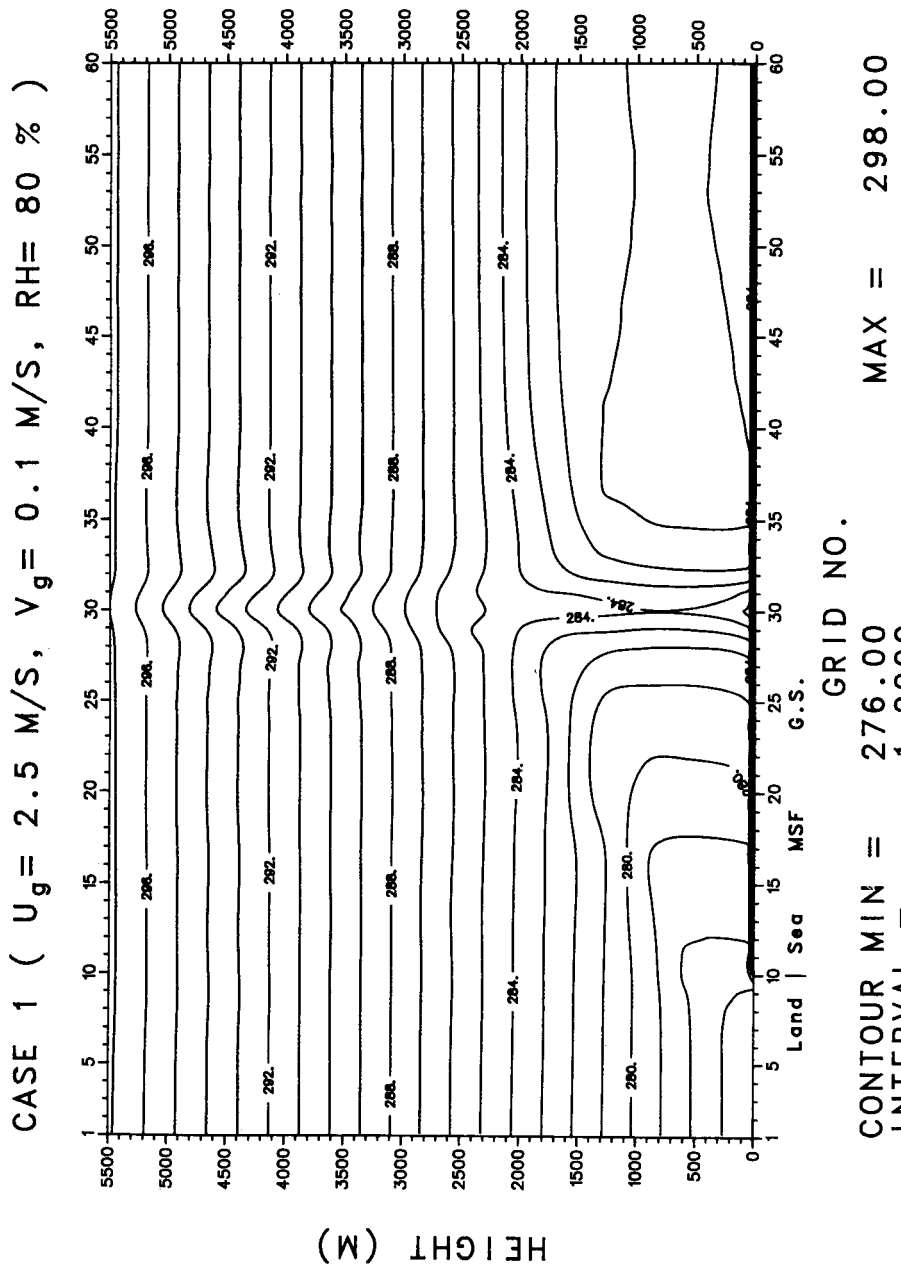

Fig. 4a. Contours of potential temperature of Case 1 (see Section 2.9) at 7 hr after the sea surface temperature was fixed. Contour information is plotted in the map and other details are the same as in Figure 1.

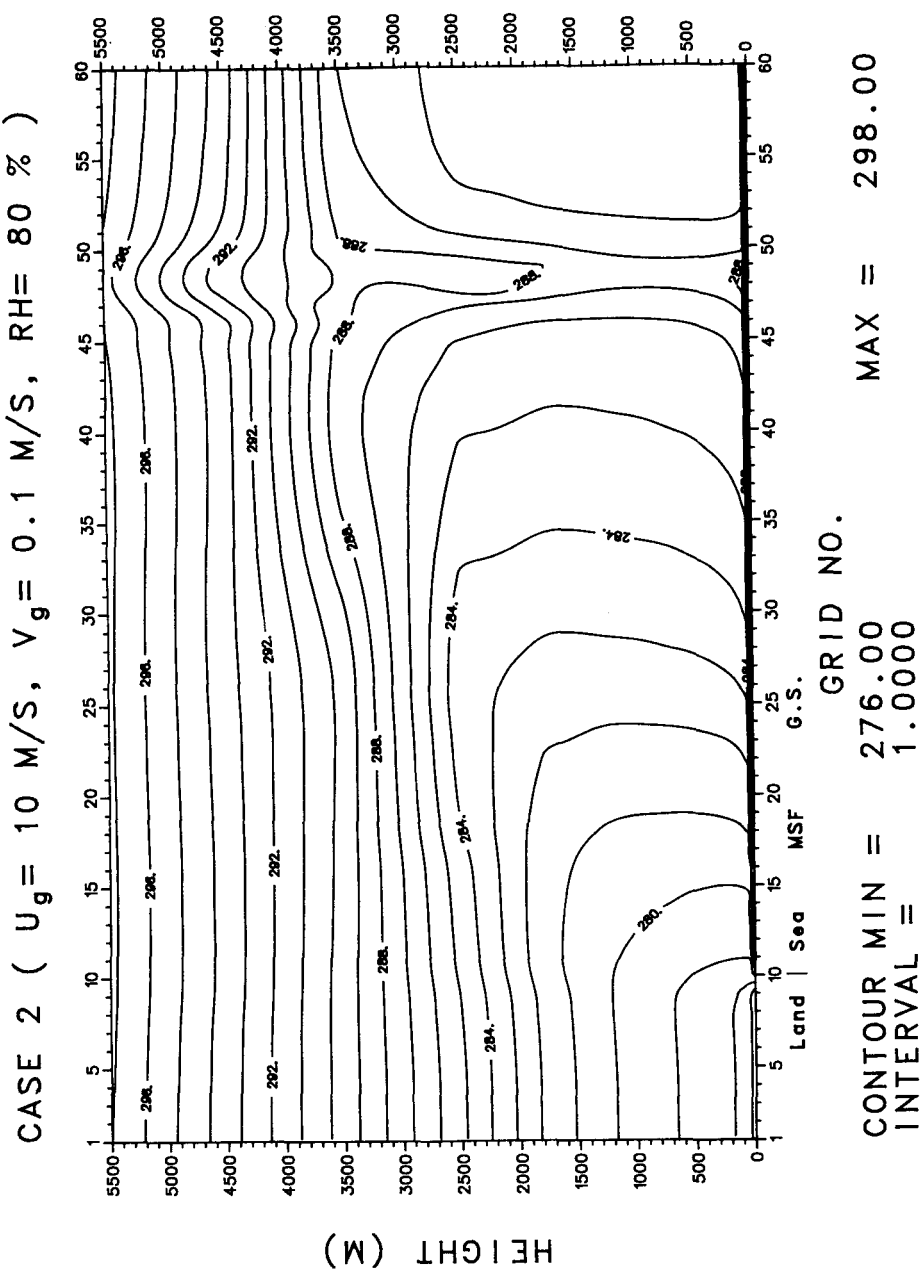

Fig. 4b. Same as Figure 4a but for Case 2 (see Section 2.9).

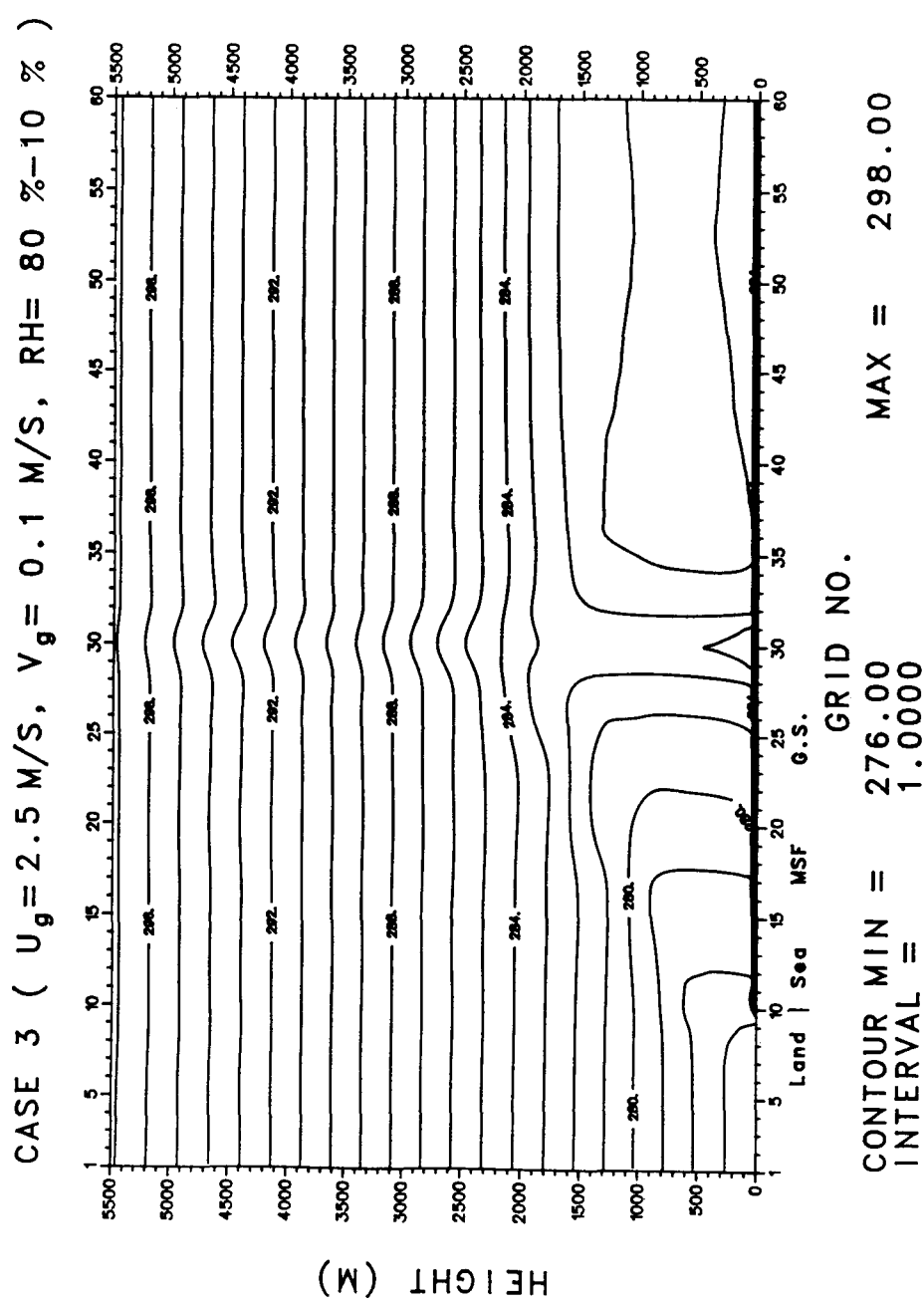

Fig. 4c. Same as Figure 4a but for Case 3 (see Section 2.9).

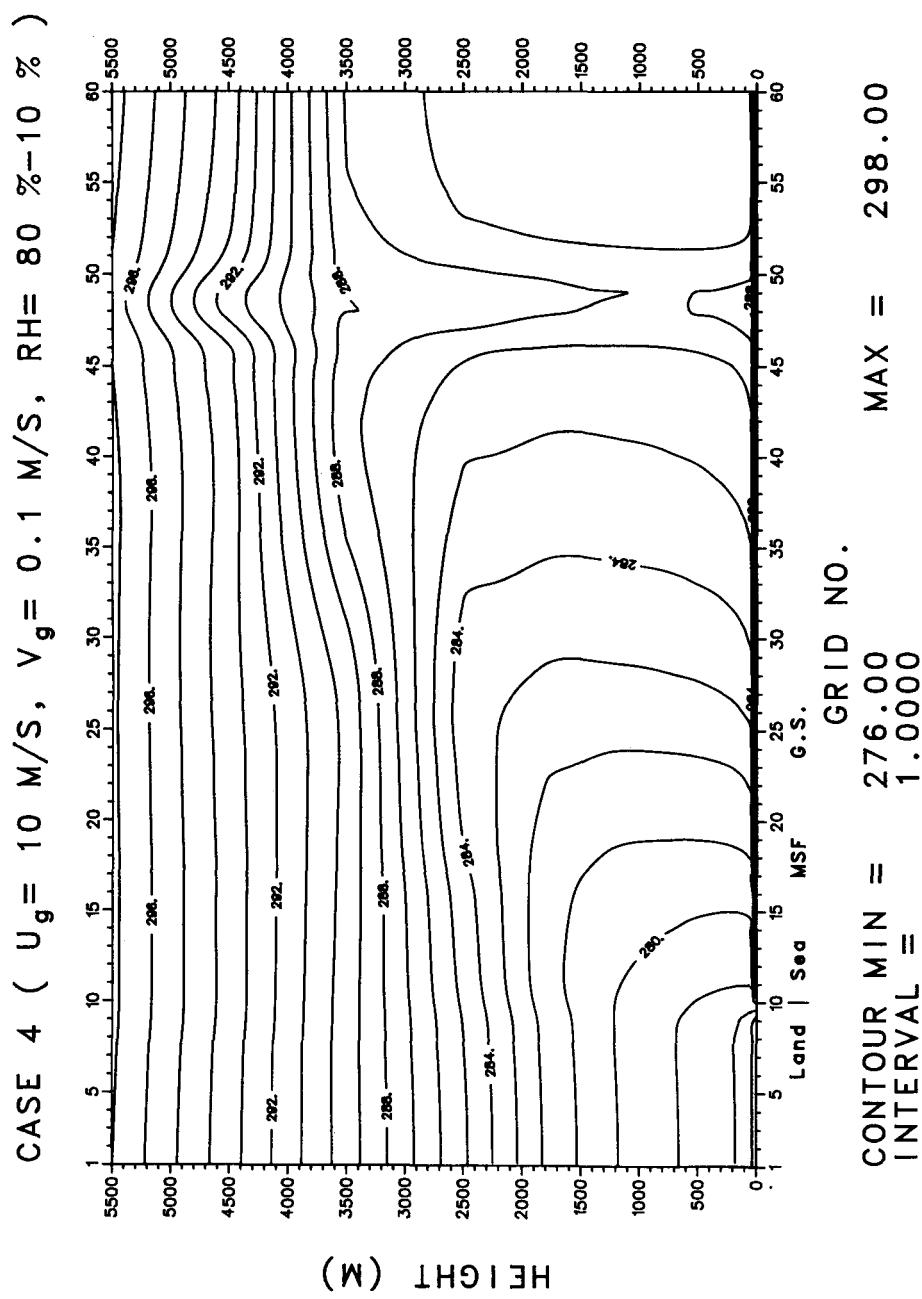

Fig. 4d. Same as Figure 4a but for Case 4 (see Section 2.9).

contrast in air-sea temperature still exists even at locations of quasi-equilibrium conditions. The degree of air mass modification at lower levels of the PBL is not significantly related to the initial wind speed because of the aerodynamic mixing processes occurring near the sea surface. Similar thermodynamic structures of highly convective PBL induced by a typical diurnal variation in land surface temperature were obtained by other investigators (e.g., Mahrer and Pielke, 1978). Others (e.g., Physick, 1978; Anthes, 1978) show vertically tilting structure of the PBL over the warmer surface. Differences between various model results are believed to be due to the initial geostrophic conditions and the choice of the parameterization schemes. Deardorff's formula for the PBL height z_i and the specification of the eddy diffusivity using O'Brien's interpolation in the present model reflect the fact that air gets well mixed over the warmer surface even under conditions of low wind speeds.

3.3. Precipitation patterns

Amounts of precipitation associated with each case are shown in Figure 5. The maximum amount of precipitation (about 3.5 mm is seen for Case 2 (U_g = 10 m s^{-1} and RH = 80%) at about 220 km downwind of the western edge of the Gulf Stream. For Case 1 (U_g = 2.5 m s^{-1} and RH = 80%), the precipitation is only about 2.6 mm but occurs closer to the western edge (about 40 km downwind) of the Gulf Stream. For both cases, precipitation is associated with regions of convergence and strong vertical motion (see Figure 2a to 2b). Quasi-stationary rainbands associated with strong convection over the Gulf Stream have been observed during GALE (Hobbs, 1987) and these are obviously the result of low level convergence caused by surface temperature discontinuities. For the linearly decreasing RH with two different geostrophic winds (2.5 m s^{-1} and 10 m s^{-1}), precipitation in the model domain is relatively small. Thus moist air advection appears to be a necessary precondition for the occurrence of precipitation. This is somewhat similar to thunderstorms and precipitation associated with sea breeze flow over Florida (Pielke, 1974a).

The precipitation pattern in a breeze-type circulation is a good indicator of the shifting of the location of maximum vertical velocity. Wider bands of precipitation are observed in Cases 2 and 4, both with a higher wind speed, while cases 1 and 3 with a lower wind speed show a more concentrated region of precipitation. The regions of precipitation occur downwind of the western edge of the Gulf Stream in all cases, which implies that the Gulf Stream is the major source of heat and moisture fluxes. The leading edge of the precipitation distribution following which the vertical velocities are negligible also indicates the maximum wet penetration determined by the low level convergence in the PBL. Some lake-breeze studies (e.g., Physick, 1976) report a maximum dry penetration of more than 200 km.

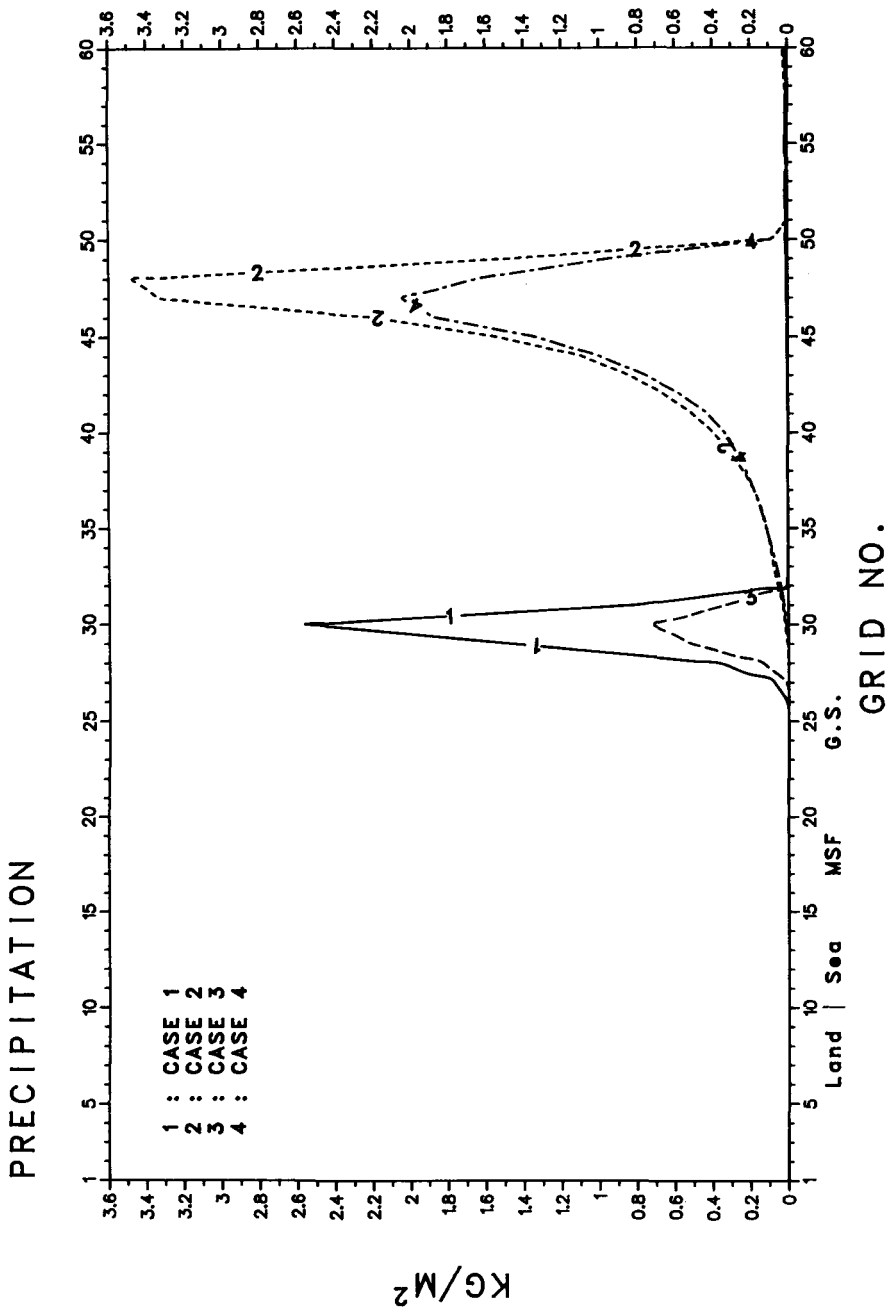

Fig. 5. Precipitation for the four cases (see Section 2.9) predicted at 7 hr after the sea surface temperature was fixed.

3.4. Variation of surface turbulent heat fluxes

Spatial variation of the surface turbulent sensible heat flux is shown in Figure 6 for different cases. Larger fluxes are seen for higher geostrophic winds with sharp increases at sea surface temperature discontinuities. This is due to increased wind speeds caused by the acceleration effect of the convergence process. Several buoys were deployed along the Carolina coast during GALE to monitor basic meteorological parameters (Raman and Riordan, 1988). A typical sensible heat flux of about 500 $W m^{-2}$ was estimated between the mid-shelf front and the Gulf Stream for the January 28 cold air outbreak (Akkarapuram and Raman, 1988). Model prediction values of about 240 $W m^{-2}$ at mid-shelf and 420 $W m^{-2}$ over the Gulf Stream are of the same order of magnitude.

Spatial variation of the surface turbulent latent heat flux is shown in Figure 7 for all four simulations. Again larger fluxes for higher geostrophic wind and step changes in values corresponding with a sea surface temperature discontinuity are apparent. Latent heat fluxes are larger than the sensible heat fluxes by a factor of about two. A typical value of about 800 $W m^{-2}$ was estimated during the January 28 cold air outbreak just east of the mid-shelf front (Akkarapuram and Raman, 1988) compared to the model values of about 450 $W m^{-2}$ at mid-shelf and 900 $W m^{-2}$ over the Gulf Stream. These comparisons have been made with the typical measured values over this area during GALE.

3.5. Spatial variation of the scaling parameters

Four scaling parameters that are important in the PBL and considered in the model are the surface friction velocity u_*, surface friction temperature θ_*, surface friction humidity q_* and the convective velocity w_*. In this section we shall discuss the spatial variation of these quantities and compare their modeled values with observations for the January 28, 1986 cold air outbreak.

Spatial variation of u_* values computed by the model is shown in Figure 8 for the four cases. As expected, high-wind simulations cause larger u_* in the entire domain. Sharp increases in u_* are related to the surface temperature discontinuities and increased convection. A surface friction velocity of about 50 $cm s^{-1}$ was observed by research aircraft over the Gulf Stream at a height of about 30 m (Wayland and Raman, 1987). The model value of about 50 $cm s^{-1}$ is in good agreement with the observation. Peaks of u_* values are associated with areas of convergence and the lower values of u_* with low mean winds in the divergence zones.

Spatial variation of θ_* shown in Figure 9 again follows the features of surface temperature discontinuities at the land-sea interface and the mid-shelf front. High wind cases (Cases 2 and 4) differ from the low wind ones (Cases 1 and 3), particularly over the Gulf Stream. The lower values of $-\theta_*$ for Cases 2 and 3 are believed to be due to the smaller air-sea temperature difference caused by increased convection accompanying large sensible heat fluxes. The spatial varia-

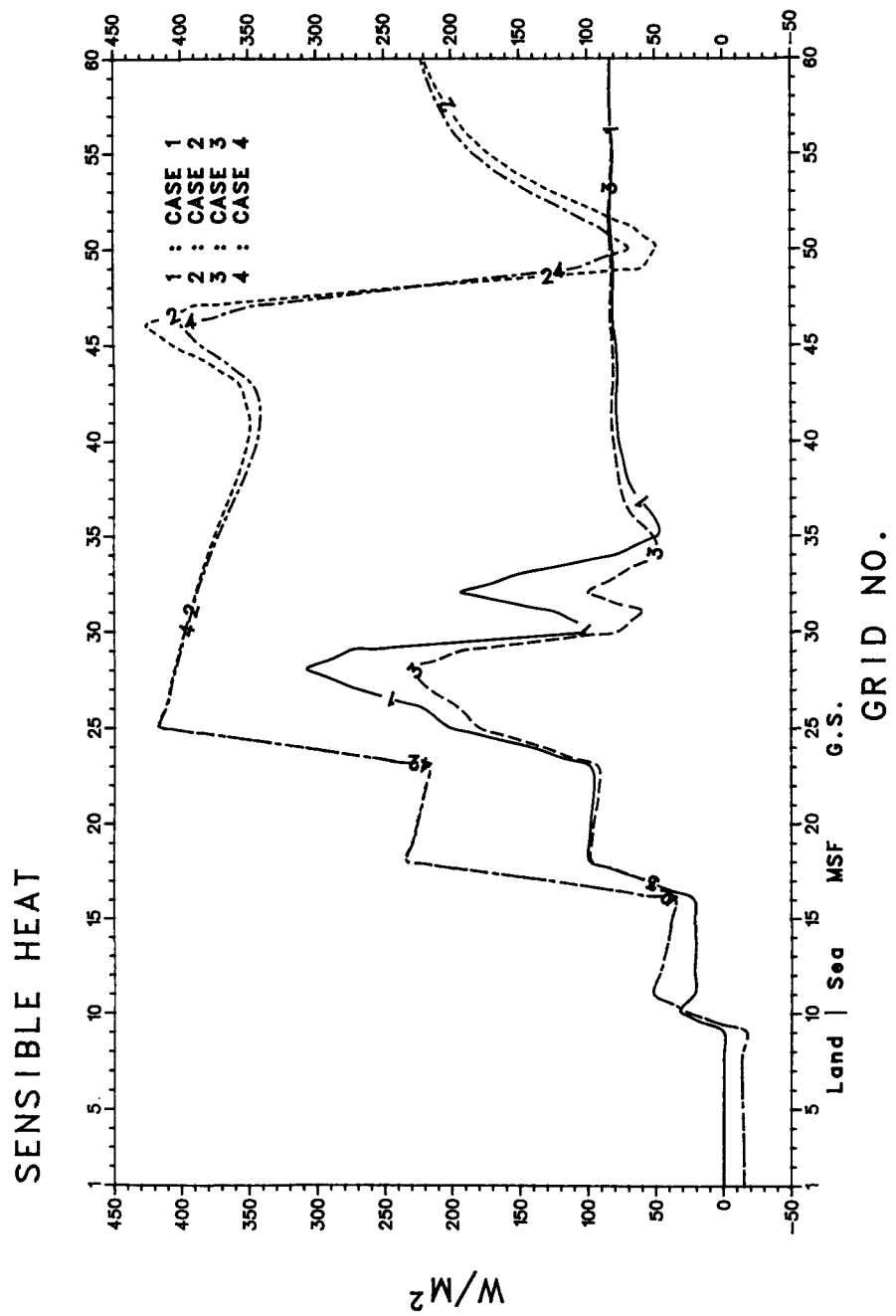

Fig. 6. Sensible heat flux for the four cases (see Section 2.9) computed at 7 hr after the sea surface temperature was fixed.

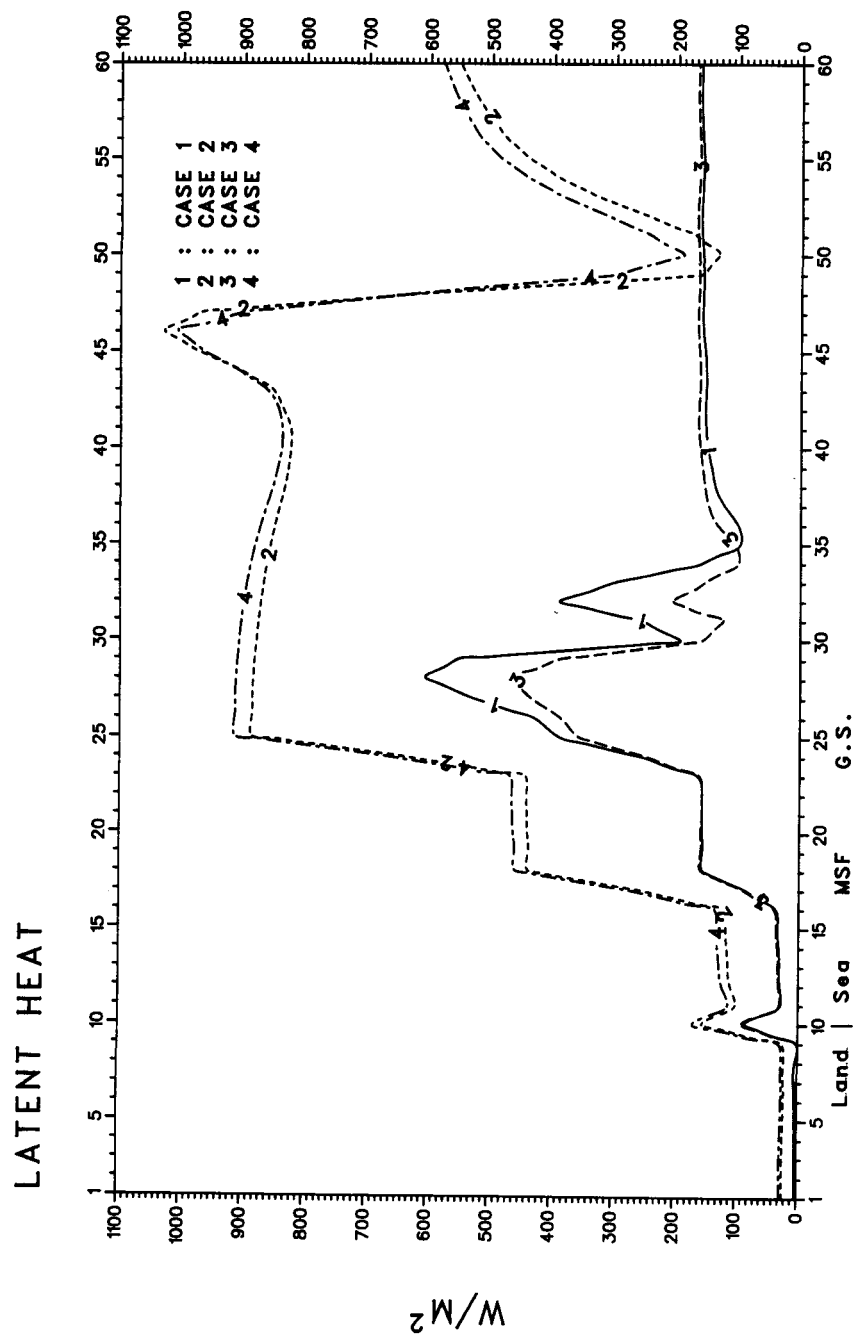

Fig. 7. Latent heat flux for the four cases (see Section 2.9) computed at 7 hr after the sea surface temperature was fixed.

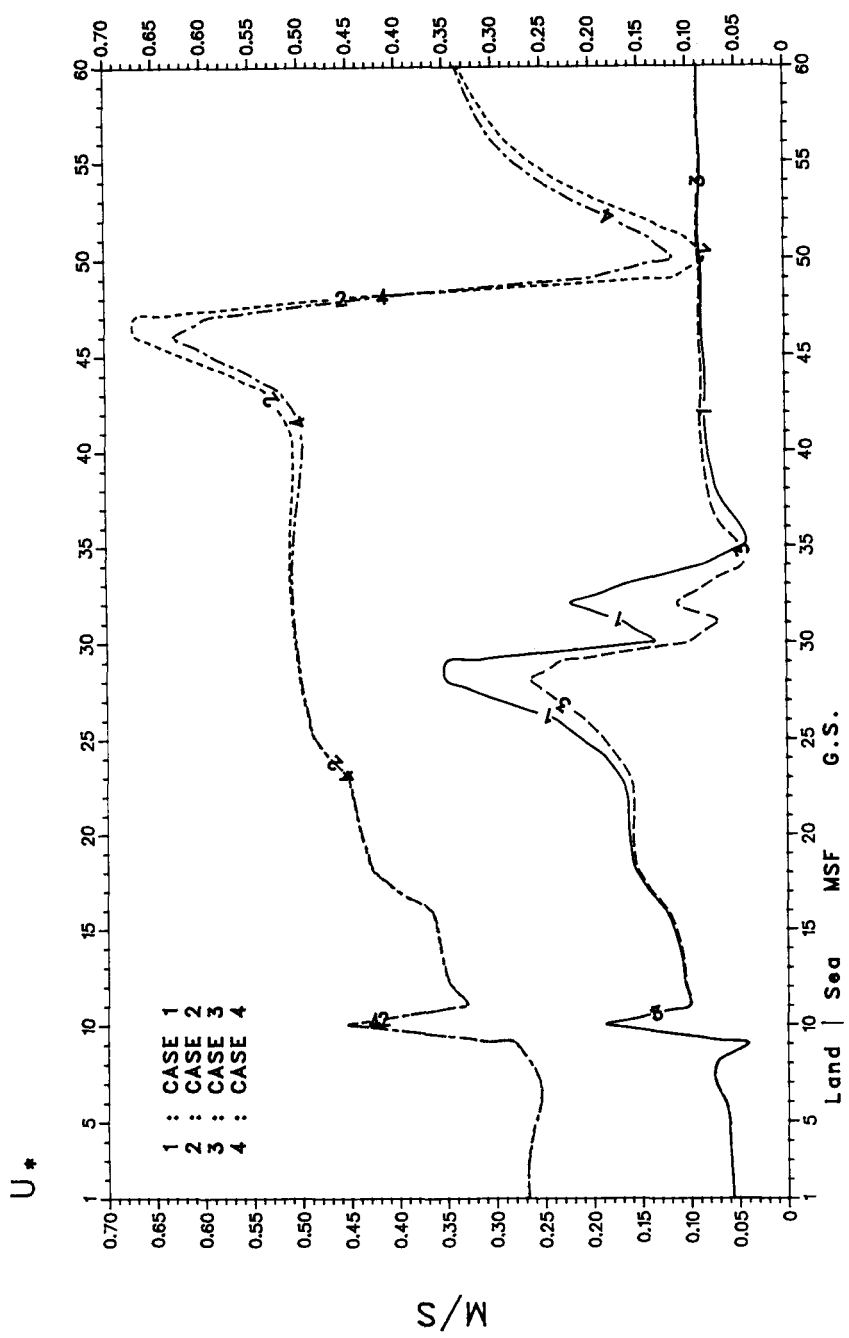

Fig. 8. Surface friction velocity for the four cases (see Section 2.9) computed at 7 hr after the sea surface temperature was fixed.

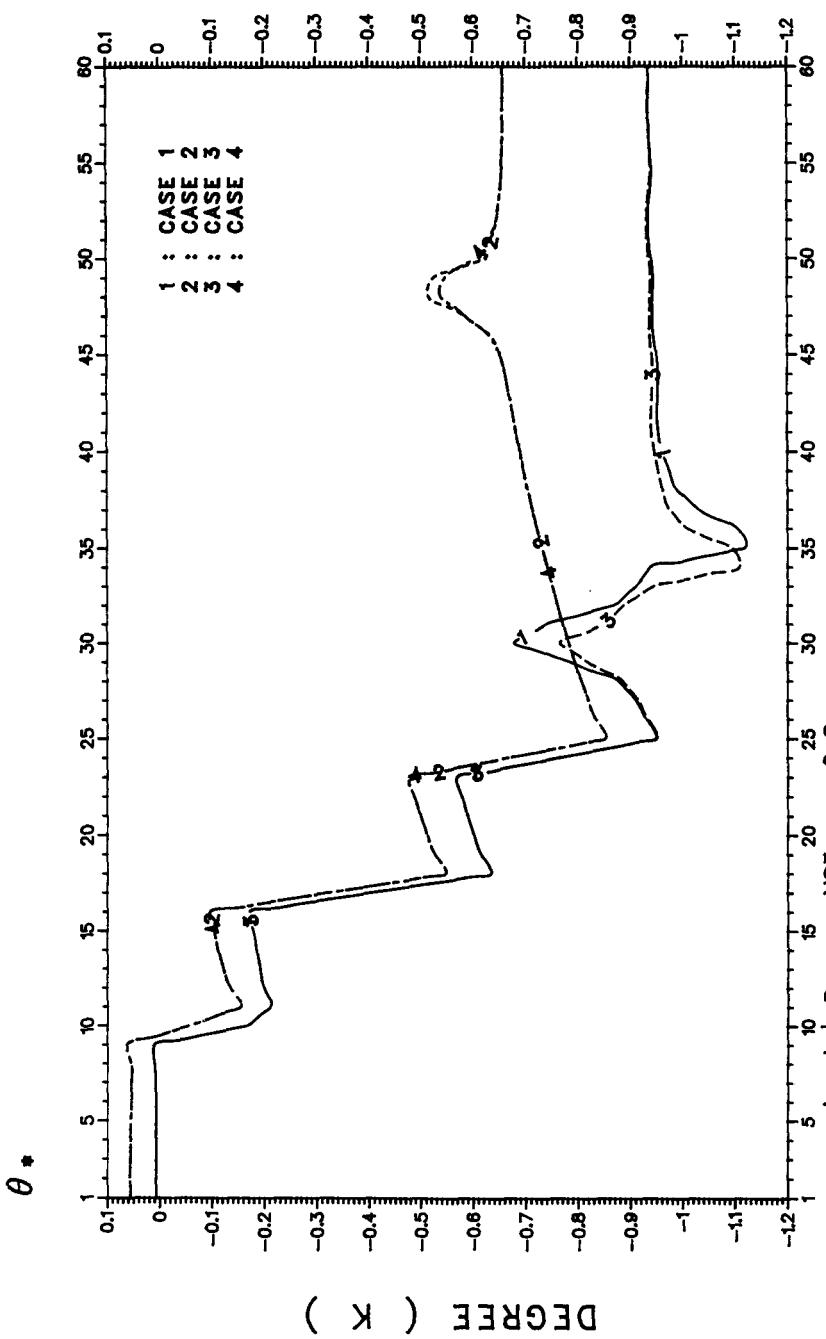

Fig. 9. Surface flux temperature for the four cases (see Section 2.9) computed at 7 hr after the sea surface temperature was fixed.

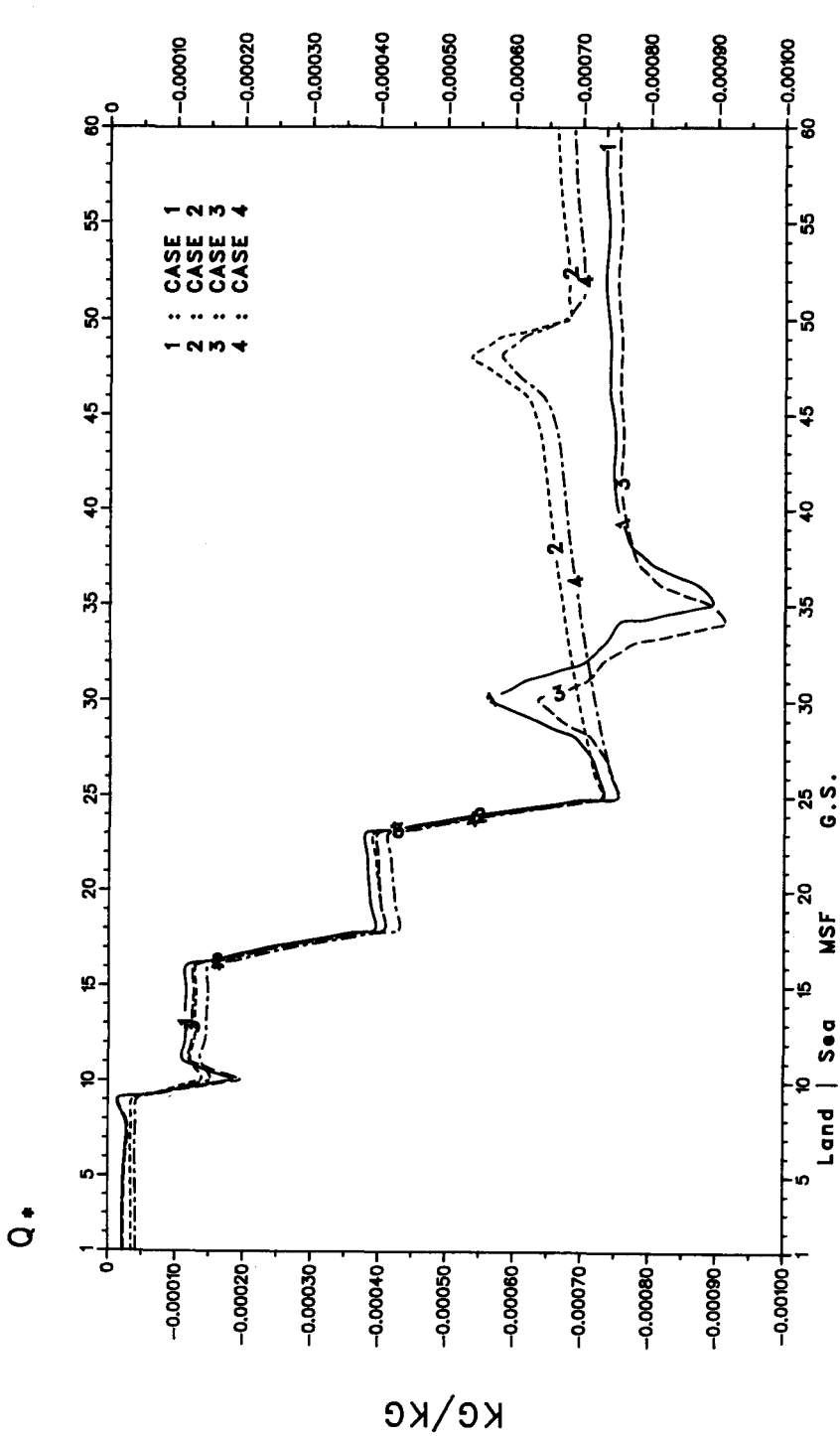

Fig. 10. Surface flux moisture for the four cases (see Section 2.9) computed at 7 hr after the sea surface temperature was fixed.

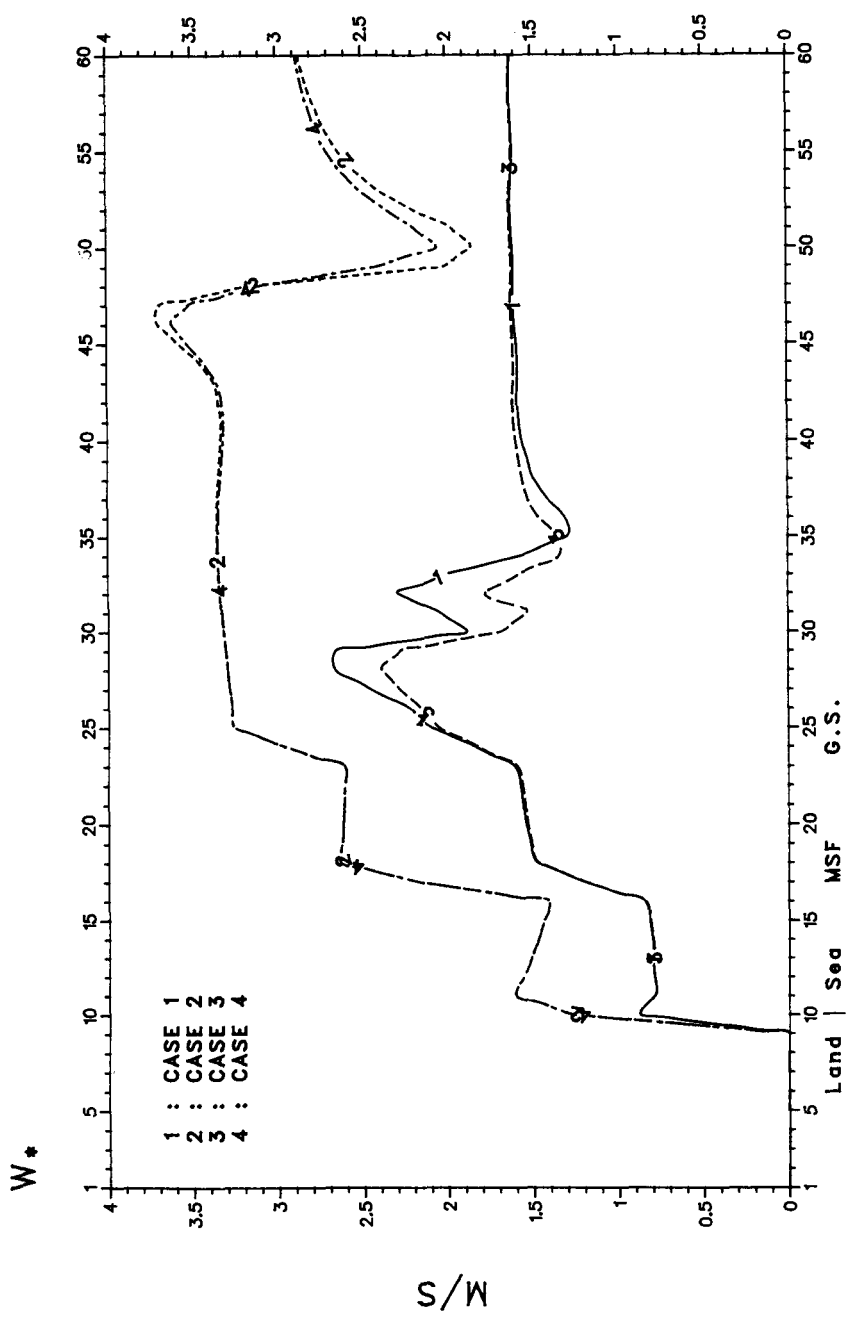

Fig. 11. Convective velocity for the four cases (see Section 2.9) computed at 7 hr after the sea surface temperature was fixed.

tion of q_* shown in Figure 10 is essentially similar to θ_* except for the clear delineation over the Gulf Stream. Effect of the sharp surface temperature discontinuities on q_* is seen at the land-sea interface and the mid-shelf front. Over the Gulf Stream, a minimum $-q_*$ is obtained for lower geostrophic wind. With larger geostrophic wind, $|q_*|$ decreases again possibly due to increased mixing.

Variation of the convective velocity scale w_* for the four cases is shown in Figure 11. The variations for different simulations are somewhat similar to the u_* distribution shown in Figure 8 with the difference that w_* values are still large even in the areas of divergence and low mean wind speed. The w_* values over the Gulf Stream are larger than the mean vertical velocities indicating significant contributions by subgrid scale processes. Convective velocity over the Gulf Stream was estimated to be about 2.7 m s^{-1} for the intense cold air outbreak on January 28, 1986 (Wayland and Raman, 1987) using aircraft data. Model values of about 3.3 m s^{-1} are in good agreement with the observations.

4. Conclusions

Four different simulations of cold air advection over the Gulf Stream were considered using a mesoscale numerical model. Sea surface temperature distribution was selected to conform with the typical variation normally observed off the Carolinas during the winter season. Effects of the magnitude of the geostrophic wind and the initial moisture of the air mass on land breeze-type circulation that develops over the Gulf Stream were examined.

Results indicate that the SST discontinuity at the western edge of the Gulf Stream dominates the convergence that occurs downwind. Stronger convergence occurs for higher geostrophic wind speed and initial moist flow. Larger sensible and latent heat fluxes also occur for this simulation, with significant precipitation. A lower geostrophic wind speed but with initially moist air also produces precipitation over the Gulf Stream. When the air is initially relatively drier, the vertical velocities over the Gulf Stream are weaker and the precipitation is insignificant. Model results concerning the convergence of wind, vertical velocities, friction velocity, convective velocity scale, sensible heat flux, latent heat flux and precipitation patterns are all in reasonable agreement with observations made during GALE cold air outbreaks.

Numerically, several control experiments were conducted and they have shown that a selective smoothing is important, especially for a developing physical system with a scale equivalent to the scale of several grid lengths. A refinement of the parameterization scheme used in this numerical study will be of interest. Since the breeze-type circulation is essentially shallow but strong in the PBL and depends on subgrid turbulent processes profoundly, higher order schemes such as a turbulent energy closure scheme or a second-order closure scheme probably

will provide better for the simulation of the cold air advection over a warmer surface.

Acknowledgements

Authors would like to thank Dr Y. L. Lin for his permission to use the microVAX computer. This work was supported by the National Science Foundation under grant ATM-83-11812.

Appendix

LIST OF SYMBOLS

u	east-west velocity [m s^{-1}]
v	north-south velocity [m s^{-1}]
$\tilde{w}$	vertical velocity in σ coordinate [m s^{-1}]
w	vertical velocity in z coordinate [m s^{-1}]
θ	potential temperature [K]
q	moisture [kg kg^{-1}]
π	scaled pressure [J kg^{-1} K^{-1}]
U_g	the east-south component of geostrophic wind [m s^{-1}]
V_g	the north-south component of geostrophic wind [m s^{-1}]
σ	vertical coordinate following terrain
x	east-west spatial coordinate [m]
y	north-south spatial coordinate [m]
z	vertical spatial coordinate [m]
t	time coordinate [s]
g	gravity [m^2 s^{-1}]
E	terrain height [m]
H	total height considered in the model [m]
q_s	saturated moisture [kg kg^{-1}]
p	pressure [mb]
p_{00}	reference pressure [mb]
P	precipitation [kg m^{-2}]
γ	vertical lapse rate for potential temperature [K km^{-1}]
L	latent heat of condensation [J kg^{-1}]
C_p	specific heat at constant pressure [J kg^{-1} K^{-1}]
R	gas constant for dry air [J kg^{-1} K^{-1}]
R_v	gas constant for water vapor [J kg^{-1} K^{-1}]
f	Coriolis parameter ($2\Omega \sin \Phi$) [s^{-1}]
Ω	angular velocity of the earth [s^{-1}]
Φ	latitude [°]
K_H	horizontal eddy exchange coefficient [m^2 s^{-1}]
Δt	integration time interval [s]
Δx	grid interval distance in x coordinate [m]
Δy	grid interval distance in y coordinate [m]
α	adjustable coefficient in K_H
$\overline{u'w'}$	subgrid momentum flux [m^2 s^{-2}]
$\overline{w'\theta'}$	subgrid potential temperature flux [m K s^{-1}]
$\overline{w'q'}$	subgrid moisture flux [m kg kg^{-1} s^{-1}]
u_*	friction velocity [m s^{-1}]
θ_*	subgrid flux temperature [K]

q_* subgrid flux moisture [kg kg^{-1}]
w_* subgrid convective velocity [m s^{-1}]
z_0 surface roughness [m]
L Monin stability length [m]
θ_s surface potential temperature [K]
k von Karman's constant (0.4)
ν air kinematic viscosity coefficient [m^2 s^{-1}]
K_M subgrid vertical eddy exchange coefficient for momentum [m^2 s^{-1}]
K_θ subgrid vertical eddy exchange coefficient for heat [m^2 s^{-1}]
K_q subgrid vertical eddy exchange coefficient for moisture [m^2 s^{-1}]
z_i the height of PBL [m]
h_s the height of surface layer [m]

References

Akkarapuram, A. F. and Sethu Raman: 1988, 'A Comparison of Friction Velocities Obtained Using Dissipation Method with an Iterative-Type Bulk Aerodynamic Method Using GALE Marine Observations', *Geophys. Res. Letters*, **15**, 401–404.

Anthes, R. A.: 1978, 'The Height of the Planetary Boundary Layer and the Production of Circulation in a Sea Breeze Model', *J. Atmos. Sci.* **35**, 1231–1239.

Arya, S. P. S.: 1988, *Introduction to Micrometeorology*, Academic Press, New York, (in press).

Atlas, D., Chou, S.-H., and Byerly, W. P.: 1983, 'The Influence of Coastal Shape on Winter Meso-scale Air-Sea Introduction', *Mon. Wea. Rev.* **111**, 245–252.

Blackadar, A. K. and Tennekes, H.: 1968, 'Asymptotic Similarity in Neutral Barotropic Planetary Boundary Layers', *J. Atmos. Sci.* **25**, 1015–1020.

Brown, P. S. and Pandolfo, J. P.: 1979, 'Numerical Stability of the Combined Advection-Diffusion Equation with Nonuniform Spatial Grid', *Mon. Wea. Rev.*, **107**, 959–963.

Businger, J. A., Wyngaard, J. C., Izumi, Y. and Bradley, E. F.: 1971, 'Flux-Profile Relationships in the Atmospheric Surface Layer', *J. Atmos. Sci.* **28**, 181–189.

Chou, S.-H. and Atlas, D.: 1982, 'Satellite Estimates of Ocean-Air Heat Fluxes During Cold Air Outbreak', *Mon. Wea. Rev.* **110**, 1434–1450.

Clark, R. H.: 1970, 'Recommended Methods for the Treatment of the Boundary Layer in Numerical Models', *Aust. Meteorol. Mag.* **18**, 51–73.

Cullen, M. J. P.: 1976, 'On the Use of Artificial Smoothing in Galerkin and Finite Difference Solutions of the Primitive Equations', *Q.J.R. Meteorol. Soc.* **102**, 77–93.

Deardorff, J. W.: 1966, 'The Contragradient Heat Flux in the Lower Atmosphere and in the Laboratory', *J. Atmos. Sci.* **23**, 503–506.

Deardorff, J. W.: 1974, 'Three-Dimensional Numerical Study of the Height and Mean Structure of a Heated Planetary Boundary Layer', *Boundary-Layer Meteorol.* **7**, 81–106.

Dirks, R., Kuettner, J. P., and Moore, J.: 1988, 'An Overview of the Genesis of Atlantic Lows Experiment', *Bull. Amer. Meteor. Soc.*, (in press).

Estoque, M. A.: 1961, 'A Theoretical Investigation of the Sea Breeze', *Q.J.R. Meteorol. Soc.* **87**, 136–146.

Hobbs, P. V.: 1987, 'The Gulf Stream Rainband', *Geophys. Res. Letters* **14**, 1142–45.

Huang, C. Y.: 1986, 'Numerical Simulations of the Effects of Complex Terrain on Airflow in PBL', Master thesis submitted to the Department of Atmospheric Sciences, National Taiwan University, Taipei.

Leith, 1969, 'Two Dimensional Eddy Viscosity Coefficients', *Proc. WMO/IUGG Symp. Numerical Wea. Prediction*, 26 November–4 December, 1968, Meteor. Soc. of Japan, Tokyo, 1–41 to 1–44.

Leonard, B. P.: 1979, 'A Stable and Accurate Convective Modeling Procedure Based on Quadratic Upstream Interpolation', *Comput. Methods Appl. Mech. Eng.* **19**, 59–98.

Lin, Y. L. and Smith, R. B.: 1986, 'Transient Dynamics of Airflow Near a Local Heat Source', *J. Atmos. Sci.*, **43**, 40–49.

Mahrer, Y. and Pielke, R. A.: 1978, 'A Test of an Upstream Spline Interpolation Technique for the Advective Terms in a Numerical Mesoscale Model', *Mon. Wea. Rev.* **106**, 818–830.

Marshall, R. and Sethu Raman: 1986, 'C-Band Dopper Radar Observations of the Marine Boundary Layer during GALE, Pre-print Vol. of 23rd conference on Radar Meteorology, Snowmass, CO.

McNider, R. T. and Pielke, R. A.: 1981, 'Diurnal Boundary-Layer Development over Sloping Terrain', *J. Atmos. Sci.* **38**, 2198–2212.

Miller, M. J. and Thorpe, A. J.: 1981, 'Radiation Conditions for the Lateral Boundaries of Limited Area Numerical Models', *Q.J.R. Meteorol. Soc.* **107**, 615–628.

O'Brien, J. J.: 1970, 'A Note on the Vertical Structure of the Eddy Exchange Coefficient in the Planetary Boundary Layer', *J. Atmos. Sci.* **27**, 1213–1215.

Orlanski, I.: 1976, 'A Simple Boundary Condition for Unbounded Hyperbolic Flows', *J. Comput. Phys.* **21**, 251–269.

Physick, W.: 1976, 'A Numerical Model of the Sea-Breeze Phenomenon Over a Lake of Gulf', *J. Atmos. Sci.* **33**, 2107–2135.

Pielke, R. A.: 1974a, 'A Three-Dimensional Numerical Model of the Sea Breeze over South Florida', *Mon. Wea. Rev.* **102**, 115–139.

Pielke, R. A.: 1974b, 'A Comparison of Three-Dimensional and Two-Dimensional Numerical Predictions of Sea Breeze', *J. Atmos. Sci.* **31**, 1577–1585.

Pielke, R. A.: 1984, *Mesoscale Meteorological Modeling*, Academic Press, New York, 612 pp.

Pielke, R. A. and Mahrer, Y.: 1975, 'Technique to Represent the Heated-Planetary Boundary Layer in Mesoscale Models with Coarse Vertical Resolution', *J. Atmos. Sci.* **32**, 2288–2308.

Pielke, R. A. and Mahrer, Y.: 1978, 'Verification Analysis of the University of Virginia Three-Dimensional Mesoscale Model Prediction over South Florida for July, 1973', *Mon. Wea. Rev.* **106**, 1568–1589.

Pietrafesa, L. J., Janowitz, G. S., and Whitman, P. A.: 1985', 'Physical Oceanographic Processes in the Carolina Capes',Atkinson *et al.*, (eds.), *Oceanography of the Southeastern U.S. Continental Shelf*, American Geophysical Union Monograph, 23–32.

Raman, S. and Raynor, G. S.: 1975, 'Surface Drag Coefficient Dependence on the Aerodynamic Roughness of the Sea', *J. Geophys. Res.* **80**, 4983–4988.

Raman, S., Riordan, A. J., Holt, T., Stunder, M., and Hinman, J.: 1985', Observations of the Marine Boundary Layer Thermal Structure in the Vicinity of the Gulf Stream During a Cold Air Outbreak', *J. of Climatology and Applied Meteor.* **25**, 14–21.

Raman, S. and Riordan, A. J.: 1987, 'The Genesis of Atlantic Lows Experiment (GALE): The Planetary Boundary Layer Subprogram', *Bull. Amer. Meteor. Soc.* **69**, 161–172.

Shapiro, R.: 1971, 'The Use of Linear Filtering as a Parameterization of Atmospheric Diffusion', *J. Atmos. Sci.* **28**, 523–531.

Shapiro, R.: 1975, 'Linear Filtering', *Math. Comp.* **29**, 1094–1097.

Smith, R. B. and Lin, Y. L.: 1982, 'The Addition of Heat to a Stratified Airstream with Application to the Dynamics of Orographic Rain', *Q.J.R. Meteorol. Soc.* **108**, 353–378.

Smolarkiewicz, P. K.: 1983, 'A Simple Positive Definite Advection Scheme with Small Implicit Diffusion, *Mon. Wea. Rev.* **111**, 479–486.

Sun, W. Y. and Hsu, W. R.: 1988, 'Numerical Study of a Cold Air Outbreak Over the Ocean', *J. Atmos. Sci.*, **45**, 1205–1227.

Yamada, Y. and Mellor, G.: 1975, 'A Simulation of Wangara Atmospheric Boundary Layer Data', *J. Atmos. Sci.* **12**, 2309–2329.

Wayland, R. and Raman, S.: 1987, 'Turbulent Kinetic Energy Variations in the Marine Boundary Layer During the January 28, 1986 Cold Air Outbreak', *Proceedings of the Second GALE Workshop*, Virginia Beach, November 2–6, 1987.

Zilitnkevich, S. S.: 1970, 'Dynamics of the Atmospheric Boundary Layer', *Hydrometeorol.*, Leningrad.